NEUROSCIENCE

An action potential initiation mechanism in distal axons for the control of dopamine release

Changliang Liu[1]*, Xintong Cai[1], Andreas Ritzau-Jost[2], Paul F. Kramer[3], Yulong Li[4], Zayd M. Khaliq[3], Stefan Hallermann[2], Pascal S. Kaeser[1]*

Information flow in neurons proceeds by integrating inputs in dendrites, generating action potentials near the soma, and releasing neurotransmitters from nerve terminals in the axon. We found that in the striatum, acetylcholine-releasing neurons induce action potential firing in distal dopamine axons. Spontaneous activity of cholinergic neurons produced dopamine release that extended beyond acetylcholine-signaling domains, and traveling action potentials were readily recorded from dopamine axons in response to cholinergic activation. In freely moving mice, dopamine and acetylcholine covaried with movement direction. Local inhibition of nicotinic acetylcholine receptors impaired dopamine dynamics and affected movement. Our findings uncover an endogenous mechanism for action potential initiation independent of somatodendritic integration and establish that this mechanism segregates the control of dopamine signaling between axons and somata.

Neurons receive input through dendrites and send output through axons. Although axonal function is regulated locally, it is thought that distal axons are not equipped with endogenous, physiological mechanisms for action potential induction. Midbrain dopamine neurons innervate the striatum with extensively arborized axons to regulate a wide variety of functions (*1*–*4*). Of striatal neurons, 1 to 3% are tonically active interneurons that release acetylcholine (ACh), and their axons intertwine with those of dopamine neurons (*5*, *6*). Dopamine axons express high levels of nicotinic ACh receptors (nAChRs), and synchronous activation of these receptors can drive dopamine release directly (*6*–*12*). Hence, distal dopamine axons are under local striatal control and can release dopamine independent of activity ascending from their midbrain somata. However, because the command for neurotransmitter release generally originates from the soma, fundamental questions remain as to how nAChR activation is translated into dopamine release and whether this process represents a bona fide regulation used by the dopamine system.

The striatal cholinergic system broadcasts dopamine release

We expressed GRAB$_{\mathrm{DA2m}}$ [abbreviated as GRAB$_{\mathrm{DA}}$, a D2 receptor-based dopamine sensor (*13*); GRAB, G protein–coupled receptor (GPCR) activation–based] in midbrain dopamine neurons and monitored fluorescence changes in acute striatal slices (Fig. 1A). Restricting GRAB$_{\mathrm{DA}}$ expression to dopamine axons provides a widespread sensor network in the striatum and facilitates detection because the sensors are present in the immediate vicinity of dopamine release (Fig. 1B). Dopamine release was detected in both dorsal and ventral striatum without any stimulation, and this spontaneous release was sensitive to DHβE, a blocker of β2-containing nAChRs (Fig. 1, A to E; fig. S1A; and movie S1). Release occurred stochastically and exhibited all-or-none properties: Either an event covered a large area, estimated to contain 3 million to 15 million dopamine terminals (*14*), or no release was detected (Fig. 1C and fig. S1C). Because midbrain dopamine cell bodies are absent in this striatal slice preparation, the detected release is induced without involvement of dopamine neuron somata.

Using a corresponding strategy with GRAB$_{\mathrm{ACh3.0}}$ [abbreviated as GRAB$_{\mathrm{ACh}}$, an M3-receptor-based ACh sensor (*15*)], we also detected spontaneous ACh release in both dorsal and ventral striatum, which is consistent with previous work on spontaneous ACh neuron activity (*16*). ACh release was sensitive to the sodium channel blocker tetrodotoxin (TTX) and exhibited an all-or-none pattern like that of dopamine (Fig. 1, F and G; fig. S1, A to C; and movie S2). The frequency of ACh release was approximately threefold higher than that of dopamine release, suggesting that not all ACh triggers dopamine release (Fig. 1, E and G). Although less frequent, areas covered by dopamine release were approximately three times larger compared with those of ACh (Fig. 1H). Adjusting event detection thresholds or enhancing GRAB$_{\mathrm{ACh}}$ expression by injecting the respective adeno-associated virus (AAV) directly into the striatum slightly influenced the signals (fig. S1, D to G), but dopamine release continued to be less frequent and broader than ACh release. Increasing slice thickness enhanced dopamine release frequency, but blocking synaptic transmission only marginally influenced dopamine and ACh release (fig. S2).

Cholinergic interneurons exhibit multiple firing activities: They have spontaneous pacemaker activity and respond with pause-rebound firing in vivo to a variety of sensory stimuli (*17*–*20*). Because spontaneous cholinergic activity drives dopamine release stochastically (Fig. 1, C and D), we speculated that pause-rebound firing might induce time-locked dopamine release. We mimicked ACh pause-rebound activity in striatal slices and found that it induces a robust dopamine transient during rebound firing (fig. S3).

We next evoked dopamine and ACh release using electrical stimulation (Fig. 1, I to S). A large proportion of electrically evoked dopamine release was driven by activation of nAChRs (Fig. 1, I and J) (*6*, *10*, *12*, *14*). Consistent with the findings from spontaneous release, evoked dopamine release covered an area three to four times larger than that of evoked ACh release, and nAChR blockade strongly reduced its area (Fig. 1, K and O). Similar results were obtained when ACh and dopamine release were measured simultaneously [with GRAB$_{\mathrm{ACh}}$ and rGRAB$_{\mathrm{DA1h}}$, abbreviated as rGRAB$_{\mathrm{DA}}$, a red-shifted dopamine sensor (*13*)], and the release areas were positively correlated with one another (Fig. 1, Q to S).

Dopamine release with nAChR activation depressed more strongly during repetitive stimulation than release evoked without it (Fig. 1 I to L) (*12*, *14*). This is thought to be a result of rapid nAChR desensitization, but our data indicate that it is most likely caused by depression of ACh release after the first stimulus (Fig. 1, M to P). The depression of ACh release was attenuated by blocking nAChRs or D2 receptors, but not AMPA, *N*-methyl-D-aspartate (NMDA), or γ-aminobutyric acid type A (GABA$_{\mathrm{A}}$) receptors (Fig. 1P and fig. S4, A to D), suggesting that it is due to feedback inhibition mediated by dopamine. Blocking nAChRs or D2 receptors also increased ACh release in response to the first stimulus (Fig. 1, M to O, and fig. S4, E to G), likely because ACh release is tonically inhibited by dopamine (*18*).

ACh- and action potential–induced dopamine secretion share release mechanisms

We next asked why dopamine release spreads beyond the area of ACh release (Fig. 1, Q to S). We first examined the organization of striatal ACh terminals and dopamine axons using superresolution three-dimensional structured illumination microscopy (3D-SIM). Although synaptophysin-tdTomato–labeled ACh terminals were intermingled with tyrosine hydroxylase (TH)–labeled dopamine axons, no prominent association was detected (*8*, *21*), and their contact frequency was much lower than the density of release sites in dopamine axons (Fig. 2, A and B) (*14*).

Dopamine axons contain varicosities that are filled with vesicles, but only a small fraction

---

[1]Department of Neurobiology, Harvard Medical School, Boston, MA, USA. [2]Carl-Ludwig-Institute of Physiology, Faculty of Medicine, Leipzig University, Leipzig, Germany. [3]Cellular Neurophysiology Section, National Institute of Neurological Disorders and Stroke, National Institutes of Health, Bethesda, MD, USA. [4]State Key Laboratory of Membrane Biology, Peking University School of Life Sciences, Beijing, China.
***Corresponding author. Email: changliang_liu@hms.harvard.edu (C.L.); kaeser@hms.harvard.edu (P.S.K.)**

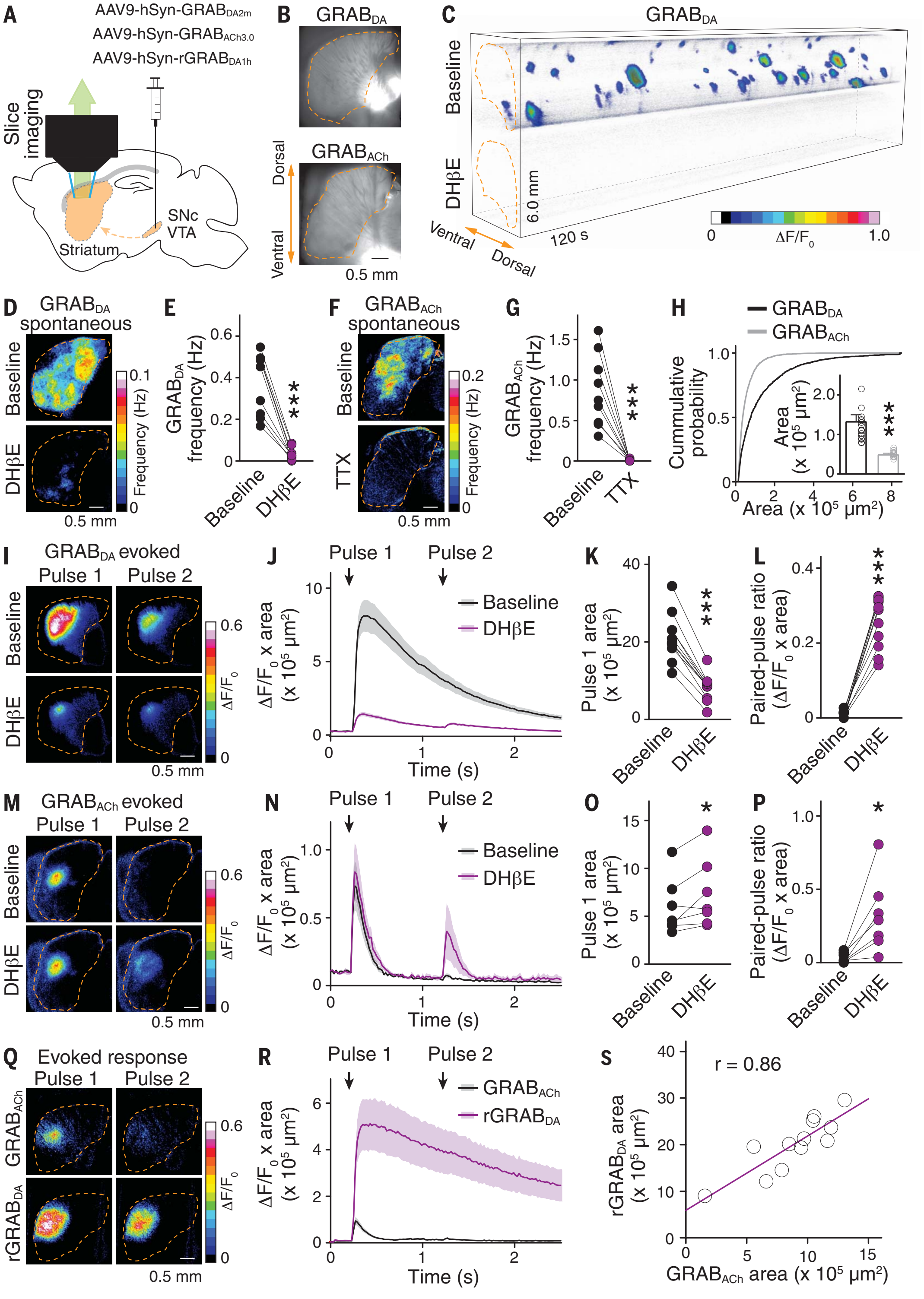

Fig. 1. ACh-induced dopamine secretion expands beyond ACh release. (**A**) Schematic of midbrain AAV injection for dopamine axonal expression of GRAB$_{DA}$, rGRAB$_{DA}$, or GRAB$_{ACh}$ sensors followed by widefield fluorescence imaging in parasagittal striatal slices. (**B**) GRAB$_{DA}$ and GRAB$_{ACh}$ expression in striatal slices. Dashed lines (orange) outline the striatum. (**C**) Volume-rendered time series of spontaneous GRAB$_{DA}$ fluctuations (expressed as $\Delta F/F_0$, color-coded for magnitude) before (top) and after (bottom) application of DHβE (1 µM). Areas with $\Delta F/F_0 < 0.02$ were made transparent for clarity. (**D**) Example frequency maps and (**E**) quantification of spontaneous GRAB$_{DA}$ events detected before and after 1 µM DHβE; *n* = 9 slices from four mice. (**F** and **G**) As in (D) and (E) but for GRAB$_{ACh}$ before and after 1 µM TTX; *n* = 9 slices from three mice. (**H**) Comparison of the area covered by GRAB$_{DA}$ and GRAB$_{ACh}$ events; *n* = 1010 events from 17 slices from four mice for GRAB$_{DA}$, *n* = 2087 events from 14 slices from four mice for GRAB$_{ACh}$. (**I**) Example images and (**J** to **L**) quantification of GRAB$_{DA}$ fluorescence evoked by paired electrical stimuli (1-s interval) before and after 1 µM DhβE; *n* = 11 slices from four mice. (**M** to **P**) As I to L, but for GRAB$_{ACh}$; *n* = 7 slices from three mice. (**Q** and **R**) As in (I) and (J) but for simultaneous assessment of GRAB$_{ACh}$ and rGRAB$_{DA}$; *n* = 12 slices from four mice. (**S**) Correlation of areas in (R). Data are mean ± SEM; $^*P < 0.05$, $^{***}P < 0.001$; Wilcoxon signed-rank tests for (E), (G), (K), (L), (O), and (P); Mann-Whitney rank-sum test for (H).

of the vesicles are releasable, and only a subset of the varicosities contains active release sites to respond to action potentials (*3*, *14*, *22*). Thus, one way for ACh neurons to boost dopamine release could be by recruiting additional vesicles and/or release sites. To test this possibility, we performed cross-depletion experiments. We expressed the light-activated cation channel channelrhodopsin-2 (ChR2) in dopamine axons and evoked dopamine release with light (to specifically activate dopamine axons) followed by electrical stimulation (to activate dopamine axons and ACh neurons) (Fig. 2C). Electrical stimulation induces dopamine release with two phases (fig. S5), and the second phase is entirely mediated by ACh (*12*, *14*). Preceding light stimulation nearly abolished the second phase (Fig. 2, D and E), indicating that vesicles and release sites are shared between the two release modes.

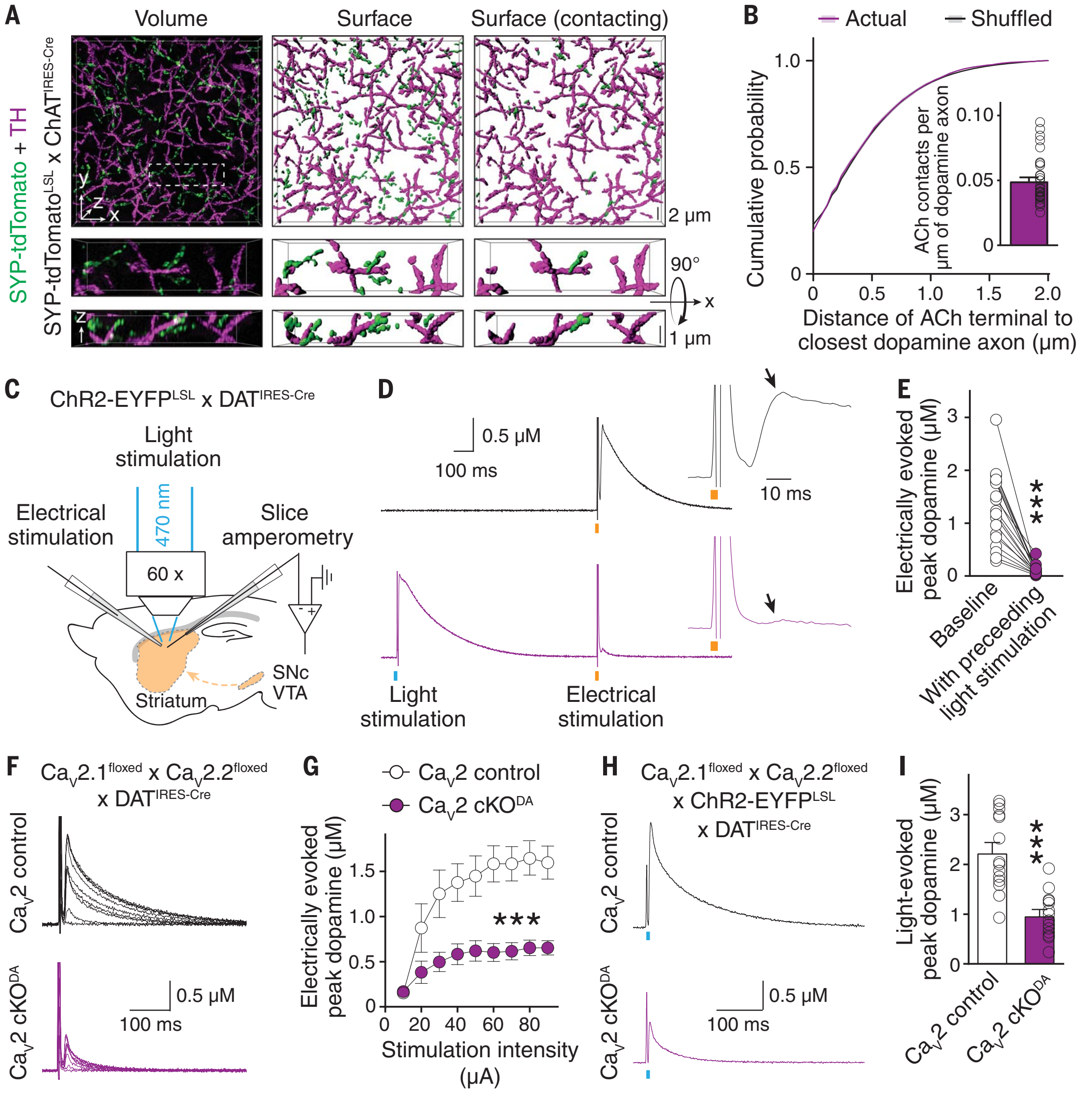

Fig. 2. ACh triggers dopamine secretion through the same release mechanisms as dopamine neuron action potentials. (**A**) Example 3D-SIM images of dorsal striatal slices showing dopamine axons (labeled with TH antibodies) and ACh nerve terminals [labeled by crossing Cre-dependent Synpatophysin-tdTomato mice (SYP-tdTomato^{LSL}) with ChAT$^{IRES-Cre}$ mice]. Images were obtained by means of (left) volume rendering of an image stack, (middle) surface rendering of detected objects, and (right) surface rendering of ACh terminals that contact dopamine axons (>0 voxel overlap). (**B**) Comparison of the minimal distance of ACh terminals from the nearest dopamine axons. Controls were generated by averaging 1000 rounds of local shuffling and distance calculation of each ACh terminal within 5 by 5 by 1 µm^3; n = 5482 objects from 33 images from four mice. (**C**) Schematic of slice recordings. ChR2-EYFP was expressed in dopamine neurons (by crossing ChR2-EYFP^{LSL} with DAT$^{IRES-Cre}$ mice), and dopamine release was measured by using amperometry in dorsal striatal slices in the area of light stimulation. (**D**) Example traces and (**E**) quantification of peak amplitude of the second dopamine release phase (arrows) evoked by means of electrical stimulation (orange bar) with (bottom) or without (top) a preceding 1-ms light stimulus (blue bar; 1 s before); n = 18 slices from three mice. (**F**) Example traces and (**G**) quantification of peak dopamine amplitude (second phase) evoked by means of electrical stimulation in Ca$_V$2 cKO^{DA} mice (Ca$_V$2.1 + 2.2 double floxed mice crossed to DAT$^{IRES-Cre}$ mice) and sibling Ca$_V$2 control mice; n = 13 slices from four mice each [$P < 0.001$ for genotype, stimulation intensity and interaction; two-way analysis of variance (ANOVA); genotype effect reported in the figure]. (**H** and **I**) Similar to (F) and (G) but with dopamine release evoked by means of light stimulation in mice expressing ChR2-EYFP transgenically in dopamine neurons; n = 14 slices from five mice each. Data are mean ± SEM; ***$P <$ 0.001; Kolmogorov-Smirnov test for (B); Wilcoxon signed-rank test for (E); and Mann-Whitney rank-sum test for (I).

In principle, ACh may trigger dopamine release in three ways. First, because nAChRs [including the α6- and α4-containing nAChRs on dopamine axons (*8*)] are nonselective cation channels (*23*), Ca^{2+} entry through them might directly trigger dopamine vesicle fusion. Second, nAChR activation might depolarize the dopamine axon membrane and activate low-voltage–gated Ca^{2+} channels to induce dopamine release. Last, nAChR activation on dopamine axons might initiate ectopic action potentials followed by opening of low- and high-voltage–gated Ca^{2+} channels and release.

We started distinguishing between these possibilities by characterizing the Ca^{2+} sources for ACh-induced dopamine release. Double removal of Ca$_V$2.1 (P/Q-type) and Ca$_V$2.2 (N-type) channels in dopamine neurons similarly reduced ACh-induced release (the second phase in response to electrical stimulation) and action potential-induced release (by optogenetic activation of dopamine axons) (Fig. 2, F to I, and fig. S5A). Removing Ca$_V$2.3 (R-type) channels had no effect (fig. S5, B to D). Hence, both release modes rely on these voltage-gated Ca^{2+} channels to a similar extent, ruling out that nAChRs are the main source of Ca^{2+} influx. Because Ca$_V$2.1 and Ca$_V$2.2 are high-voltage activated and open efficiently at membrane potentials higher than typical action potential thresholds (*24*, *25*), generating ectopic action potentials in dopamine axons is most likely necessary for ACh to induce dopamine release.

Striatal cholinergic activation induces action potential firing in distal dopamine axons

To test whether ACh can induce dopamine axon firing, we expressed ChR2 in dopamine

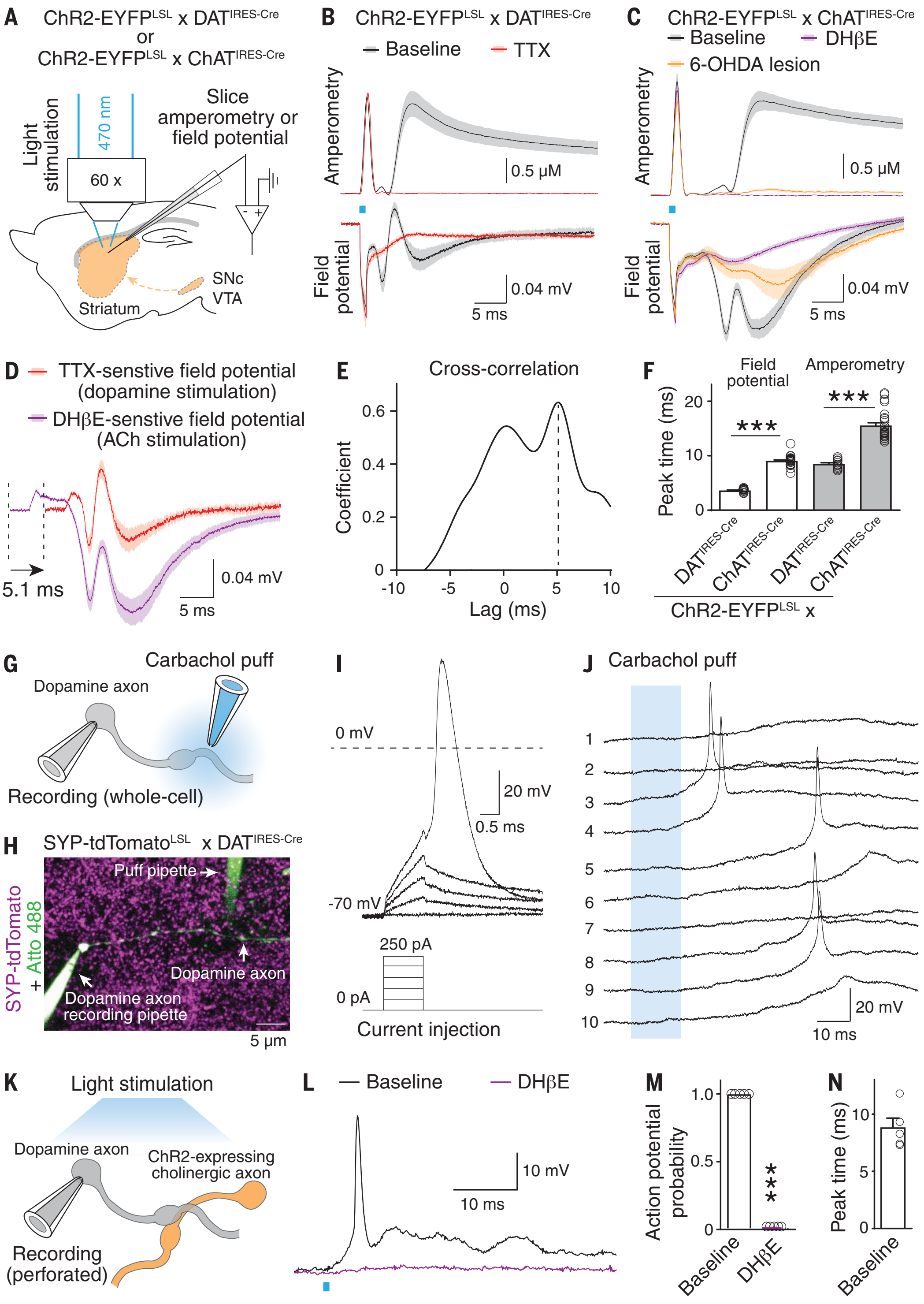

Fig. 3. Activation of nAChRs triggers action potentials in striatal dopamine axons. (**A**) Schematic of recordings with carbon fiber electrodes in voltage-clamp (0.6 V, amperometric recordings) or current-clamp (no current injection, field potential recordings). (**B** and **C**) Average traces of (top) light-evoked dopamine release (amperometry) and (bottom) field potentials in brain slices of mice with ChR2-EYFP in (B) dopamine axons or (C) ACh neurons. Example traces are provided in fig. S7, B and C. Recordings were in ACSF (baseline), (B) in 1 µM TTX, or (C) in 1 µM DHβE or (C) after 6-OHDA injection. (B) *n* = 12 slices from three mice each; (C), *n* = 25 slices from six mice (each) for baseline, *n* = 21 slices from six mice (amperometry) and *n* = 9 slices from four mice (field potentials) for DHβE, and *n* = 11 slices from six mice each for 6-OHDA. (**D**) Comparison of TTX-sensitive and DHβE-sensitive field potentials (obtained through subtraction) (fig. S7, B and C). TTX-sensitive components are right-shifted by 5.1 ms [lag detected in (E)]; *n* is as in (B) and (C). (**E**) Cross-correlation of TTX- and DHβE-sensitive components shown in (D). (**F**) Lag of peak response from the start of the light stimulus; *n* is as in (B) and (C). (**G**) Schematic and (**H**) example two-photon image of direct recording from dopamine axons. Synaptophysin-tdTomato was expressed by using mouse genetics in dopamine axons, the recorded axon was filled with Atto 488 (green) through the recording pipette, and the puff pipette contained carbachol and Atto 488. (**I** and **J**) Example responses of a dopamine axon (I) to current injections through the whole-cell pipette or (J) to 10 consecutive carbachol puffs (100 µM, numbered, 10-s intervals). (**K**) Schematic of dopamine axon perforated patch recording in mice expressing ChR2-EYFP in ACh neurons. (**L**) Example traces, (**M**) probability of action potential firing, and (**N**) lag of action potential peak times to light onset in dopamine axon recordings with optogenetic ACh interneuron activation before and after 1 µM DHβE; *n* = 5 axons from three mice. Data are mean ± SEM; ***$P < 0.001$; Kruskal-Wallis analysis of variance with post hoc Dunn's test for (F); and Mann-Whitney rank-sum test for (M).

or ACh neurons and recorded evoked dopamine release and field potentials in striatal slices using a carbon fiber electrode (Fig. 3A and fig. S6, A and B). Optogenetic activation of dopamine axons evoked robust dopamine release and a triphasic field potential that was abolished by TTX but insensitive to a range of neurotransmitter receptor blockers (Fig. 3B and fig. S7A). This indicates that the field potential represents dopamine axon population firing. Optogenetic activation of the cholinergic system produced a similar triphasic response that was disrupted by DHβE or by 6-hydroxydopamine (6-OHDA) lesion of dopamine axons (Fig. 3C and fig. S6C), demonstrating that it is evoked by nAChR activation and originates from dopamine axons.

The shape of the DHβE-sensitive component of cholinergic activation was similar to the TTX-sensitive component of dopamine axon stimulation (Fig. 3, D and E, and fig. S7, B and C), suggesting that ACh induces firing in dopamine axons. The potential induced through cholinergic activation lagged 5.1 ms behind that of dopamine axon stimulation, which is consistent with the timing of ACh-induced dopamine release (Fig. 3, D to F) (*12*, *14*). Similar to evoked ACh release (fig. S4, E to H), the field potential induced by cholinergic activation exhibited a strong depression during repetitive stimulation that was partially relieved by blocking D2 receptors (fig. S7, D and E).

To investigate the firing of individual axons, we performed direct recordings (*26*) from genetically labeled dopamine axons (Fig. 3, G and H). Current injection reliably induced large and brief action potentials (amplitude, 113 ± 2 mV; half-width, 0.64 ± 0.03 ms; n = 24 axons from nine mice) (Fig. 3I). Upon puffing of carbachol (an nAChR agonist) onto the axon 20 to 40 μm away from the recording site, 3 out of 14 axons exhibited action potential firing (Fig. 3J and fig. S7F). To test whether action potentials can be induced by endogenous ACh release, we expressed ChR2 in cholinergic interneurons and performed perforated patch recordings from dopamine axons (Fig. 3K). Optogenetic activation of ACh neurons could be tuned to evoke action potentials in all five recorded dopamine axons, and nAChR blockade abolished firing (Fig. 3, L and M). Action potential peak times matched precisely with those of the potentials measured in the field recordings (Fig. 3, F and N).

Striatal ACh and dopamine covary with movement direction

To investigate the functional relevance of ACh-induced dopamine release, we expressed $\mathrm{GRAB_{DA}}$ or $\mathrm{GRAB_{ACh}}$ together with tdTomato in the right dorsal striatum and monitored the dynamics of the corresponding transmitters by using dual-color fiber photometry in mice exploring an open field arena (Fig. 4A and fig. S8). Because striatal dopamine and ACh might play important roles in movement initiation (*27*–*31*), we aligned $\mathrm{GRAB_{DA}}$ or $\mathrm{GRAB_{ACh}}$ signals to movement onset. We found that both exhibited an increase on average, but there was strong heterogeneity in individual responses (fig. S9).

In previous studies, movement was often restricted to specific directions and/or treated as a scalar quantity (*27*–*31*). In our experiments, mice traveled freely in a large arena and constantly adjusted body posture and movement direction. If only the amplitude of velocity (speed) is considered, spatial information is lost. Hence, we treated velocity as a two-dimensional vector relative to the mouse's head orientation and registered photometry signals to the corresponding velocity plotted in polar coordinates (with angle θ defined as the direction of velocity) (Fig. 4B and fig. S10, A and D). Striatal dopamine and ACh levels were highly correlated with movement direction (Fig. 4, C and E); both exhibited an increase when the animal was turning to the contralateral side or moving forward (θ = 0° to 120°) and a decrease when the animal was turning to the ipsilateral side or backward (θ = 180° to 300°). This pattern became more evident when the time series of velocity was right-shifted (fig. S10, B and E), indicating that the velocity peak precedes that of the photometry signal.

When aligned to movement initiations with selected directions, dopamine responses diverged. There was an increase at θ = 0° to 120° and a decrease at θ = 180° to 300°, and dopamine transients peaked ~150 ms after movement onset (Fig. 4, C and D, and fig. S10, A to C). ACh levels also diverged when aligned to movement onset with selected directions. However, instead of a monotonic decrease, ACh exhibited a decrease followed immediately by an increase for movement initiations with θ = 180° to 300° (Fig. 4, E and F). This was also detected in the polar coordinates when the velocity time course was right-shifted (fig. S10, D to F).

Striatal ACh contributes to dopamine dynamics

Local inhibition of nAChRs by infusion of DHβE through the optofluid canula slightly decreased dopamine fluctuations (Fig. 4, G and H, and fig. S11, A and B). Dopamine cell bodies and the striatal cholinergic system both drive firing in dopamine axons. The effect of nAChR blockade may be limited because firing of dopamine cell bodies might dominate the signal, and somatic firing could also compensate for the loss of dopamine release induced by blocking nAChRs.

The correlation between dopamine fluctuations and movement direction was largely preserved after unilateral nAChR block with DHβE (Fig. 4I and fig. S11C). However, unilateral DHβE infusion caused a robust reduction in both amplitude and frequency of movement initiations with θ = 0° to 120°, but only a slight change in amplitude and no change in frequency of those with θ = 180° to 300° (fig. S11, D to G).

Dopamine neurons respond to salient sensory stimuli (*4*). We evoked dopamine release by applying 200-ms flashes of light to the open field arena at random intervals (Fig. 4J). Local infusion of DHβE reduced the evoked $\mathrm{GRAB_{DA}}$ response (Fig. 4K). Artificial cerebrospinal fluid (ACSF) infusion also caused a reduction, likely owing to habituation of the mice to the repeated stimuli, that was smaller than the one induced by nAChR blockade (Fig. 4L and fig. S11H). When dopamine and ACh were monitored simultaneously with $\mathrm{rGRAB_{DA}}$ and $\mathrm{GRAB_{ACh}}$, respectively, light stimulation evoked a triphasic ACh response, with the initial rise in ACh preceding that of dopamine (Fig. 4M and fig. S11I).

Discussion

Neurotransmitter release from nerve terminals is generally determined by action potentials initiated at the axon initial segment near the soma. Ectopic action potentials are less common, and their functional roles remain elusive (*32*, *33*). Here, we show that ACh induces firing in distal dopamine axons as a physiological mechanism to regulate dopamine signaling. This explains how the striatal cholinergic system broadcasts dopamine release. Ectopic action potentials likely propagate through the axonal network and trigger release along the path. This firing mechanism also accounts for the all-or-none pattern of spontaneous dopamine release and answers why coincident activity in multiple cholinergic neurons is necessary (*6*): ACh has to quickly depolarize dopamine axons to trigger action potentials before the opening of potassium channels and before ACh is degraded by acetylcholinesterase.

Axonal transmitter secretion is generally viewed to rely on the interplay between firing from the soma (which recruits the entire axon) and local regulation in single nerve terminals (which locally tunes release). We found that local ACh release not only triggers dopamine release (*6*, *9*–*12*) but hijacks the dopamine axon network to expand signaling with high temporal precision. The exceptionally high levels of nAChRs on dopamine axons (*7*, *8*) might serve to initiate axonal firing. Because presynaptic nAChRs enhance release in multiple types of neurons (*34*), this axonal firing mechanism might be important beyond the dopamine system.

Individual dopamine terminals are likely indifferent as to where an action potential is generated, and an immediate question is the functional relevance of initiating action potentials in two distinct brain areas. We propose that ACh-induced dopamine axon firing not only represents a distinct input but also sculpts a different dopamine signaling architecture compared with somatic firing. Both phasic somatic and axonal firing induction recruit groups of dopamine axons. Striatal ACh triggers action potentials in neighboring axons centered around the site of ACh release. By contrast, phasic firing in the midbrain recruits cell bodies that share excitatory input, and their axons may or may not be intermingled in the

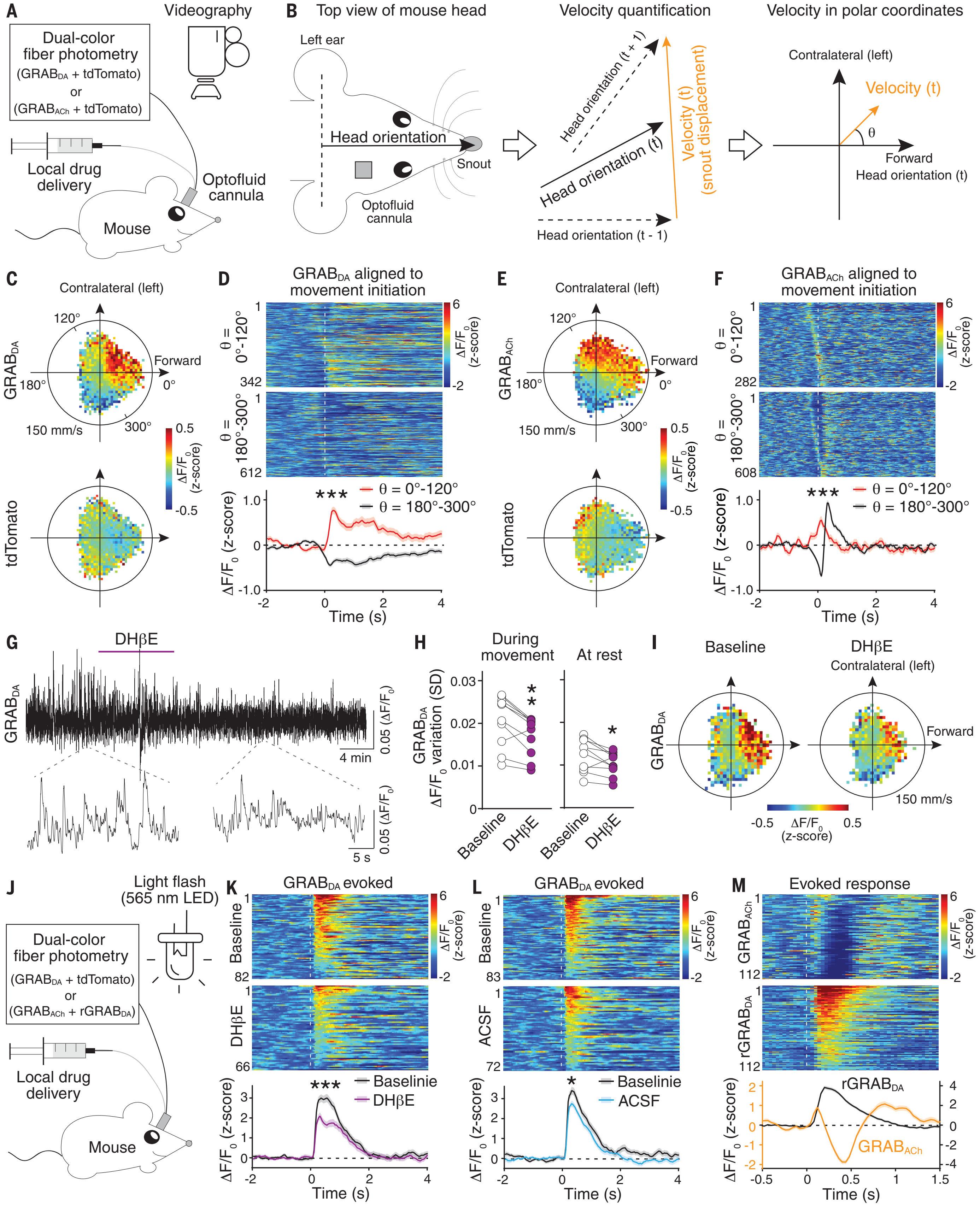

Fig. 4. Dopamine and ACh dynamics correlate with movement direction, and dopamine dynamics are attenuated after blocking nAChRs. (**A**) Strategy for simultaneous measurements of dopamine or ACh dynamics and behavior in freely moving mice. (**B**) Fiber photometry and drug delivery were in the right dorsal

striatum by using an optofluid cannula. Head orientation was defined as the direction from the center point between the ears to the snout. Instantaneous velocity at time point t was calculated from the displacement of the snout from $t - 1$ to $t + 1$ and plotted in polar coordinates with head orientation at t defined as $\theta = 0°$. (**C**) Average GRAB$_{DA}$ and tdTomato signals registered to their concurrent velocities in polar coordinates; $n = 10$ mice. (**D**) Individual (heatmap) and average GRAB$_{DA}$ fluctuations aligned to movement initiation (dashed line) with (top) $\theta = 0°$ to 120° or (bottom) 180° to 300°. Heatmaps were sorted by peak time; $n = 342$ events from 10 mice for $\theta = 0°$ to 120°, $n = 612$ events from 10 mice for $\theta = 180°$ to 300°. (**E** and **F**) As in (C) and (D) but for GRAB$_{ACh}$; $n = 282$ events from 11 mice for $\theta = 0°$ to 120°, $n = 608$ events from 11 mice for $\theta = 180°$ to 300°. (**G**) Example trace and (**H**) quantification (standard deviation of $\Delta F/F_0$) of GRAB$_{DA}$ fluorescence before and after DHβE (50 μM, 1 μl) delivered through the optofluid canula; $n = 10$ mice. (**I**) Average GRAB$_{DA}$ signals registered to concurrent velocities before and after DHβE; $n = 10$ mice. (**J**) Schematic for measurements of dopamine release induced by 200-ms light flashes in freely moving mice. (**K** and **L**) Individual (heatmap) and average GRAB$_{DA}$ fluctuations aligned to the light flash (dashed line) before and after local infusion of (K) DHβE or (L) ACSF. (K), $n = 82$ responses from 10 mice for baseline, $n = 66$ responses from 10 mice for DHβE; (L) $n = 83$ responses from 10 mice for baseline, $n = 72$ responses from 10 mice for ACSF. (**M**) Similar to (K) but for simultaneous assessment of GRAB$_{ACh}$ and rGRAB$_{DA}$; $n = 112$ responses from four mice. Data are mean ± SEM; $***P < 0.001$, $**P < 0.01$, $*P < 0.05$; Mann-Whitney rank-sum tests for areas under the curve (0 to 400 ms) in (D), (F), (K), and (L). Wilcoxon signed-rank test for (H).

striatum (*1*, *35*, *36*). Hence, ACh-induced dopamine release might endow dopamine signaling with spatial control over striatal circuitry that is distinct from release induced by activating midbrain somata. Our work further suggests that information flow in dopamine neurons between the midbrain and striatum might be bidirectional. Axon→soma signaling could occur through action potential backpropagation (*37*, *38*) upon striatal cholinergic activity to regulate somatodendritic dopamine release, dendritic excitability, or other midbrain processes.

Roles for striatal dopamine and ACh are under intense investigation, and both excitation and inhibition in the firing have been associated with spontaneous movement (*27*, *28*, *30*, *31*). We demonstrate that striatal dopamine and ACh not only correlate with movement initiation but also with its direction, potentially explaining the heterogeneity of their responses at movement onset. The findings that ACh and dopamine covary with movement direction and that ACh enhances dopamine dynamics suggest that the two systems are coordinated for their roles in motor control (*27*). These findings fit well with classical observations that unilateral lesions of dopamine or ACh systems induce asymmetric behavior and support that dynamic transmitter balance between hemispheres is important for adjusting body posture (*29*, *39*). Last, we observed that dopamine dynamics are regulated by nAChRs regardless of movement state, which indicates that ACh-induced dopamine release likely has additional physiological roles.

REFERENCES AND NOTES

1. W. Matsuda *et al.*, *J. Neurosci.* **29**, 444–453 (2009).
2. J. D. Berke, *Nat. Neurosci.* **21**, 787–793 (2018).
3. C. Liu, P. Goel, P. S. Kaeser, *Nat. Rev. Neurosci.* **22**, 345–358 (2021).
4. E. S. Bromberg-Martin, M. Matsumoto, O. Hikosaka, *Neuron* **68**, 815–834 (2010).
5. C. J. Wilson, *Neuron* **45**, 575–585 (2005).
6. S. Threlfell *et al.*, *Neuron* **75**, 58–64 (2012).
7. N. Le Novère, M. Zoli, J.-P. Changeux, *Eur. J. Neurosci.* **8**, 2428–2439 (1996).
8. I. W. Jones, J. P. Bolam, S. Wonnacott, *J. Comp. Neurol.* **439**, 235–247 (2001).
9. M. F. Giorguieff, M. L. Le Floc'h, J. Glowinski, M. J. Besson, *J. Pharmacol. Exp. Ther.* **200**, 535–544 (1977).
10. F.-M. Zhou, Y. Liang, J. A. Dani, *Nat. Neurosci.* **4**, 1224–1229 (2001).
11. R. Cachope *et al.*, *Cell Rep.* **2**, 33–41 (2012).
12. L. Wang *et al.*, *J. Physiol.* **592**, 3559–3576 (2014).
13. F. Sun *et al.*, *Nat. Methods* **17**, 1156–1166 (2020).
14. C. Liu, L. Kershberg, J. Wang, S. Schneeberger, P. S. Kaeser, *Cell* **172**, 706–718.e15 (2018).
15. M. Jing *et al.*, *Nat. Methods* **17**, 1139–1146 (2020).
16. A. A. Mamaligas, C. P. Ford, *Neuron* **91**, 574–586 (2016).
17. J. M. Schulz, M. J. Oswald, J. N. J. Reynolds, *J. Neurosci.* **31**, 11133–11143 (2011).
18. G. Morris, D. Arkadir, A. Nevet, E. Vaadia, H. Bergman, *Neuron* **43**, 133–143 (2004).
19. Y. Cai, C. P. Ford, *Cell Rep.* **25**, 3148–3157.e3 (2018).
20. C. Straub, N. X. Tritsch, N. A. Hagan, C. Gu, B. L. Sabatini, *J. Neurosci.* **34**, 8557–8569 (2014).
21. H. T. Chang, *Brain Res. Bull.* **21**, 295–304 (1988).
22. D. B. Pereira *et al.*, *Nat. Neurosci.* **19**, 578–586 (2016).
23. E. R. Decker, J. A. Dani, *J. Neurosci.* **10**, 3413–3420 (1990).
24. R. G. Held *et al.*, *Neuron* **107**, 667–683.e9 (2020).
25. J. Yang *et al.*, *Front. Cell. Neurosci.* **13**, 317 (2019).
26. A. Ritzau-Jost *et al.*, *Cell Rep.* **34**, 108612 (2021).
27. M. Howe *et al.*, *eLife* **8**, e44903 (2019).
28. P. D. Dodson *et al.*, *Proc. Natl. Acad. Sci. U.S.A.* **113**, E2180–E2188 (2016).
29. S. Kaneko *et al.*, *Science* **289**, 633–637 (2000).
30. M. W. Howe, D. A. Dombeck, *Nature* **535**, 505–510 (2016).
31. J. A. da Silva, F. Tecuapetla, V. Paixão, R. M. Costa, *Nature* **554**, 244–248 (2018).
32. T. Dugladze, D. Schmitz, M. A. Whittington, I. Vida, T. Gloveli, *Science* **336**, 1458–1461 (2012).
33. M. E. J. Sheffield, T. K. Best, B. D. Mensh, W. L. Kath, N. Spruston, *Nat. Neurosci.* **14**, 200–207 (2011).
34. J. A. Dani, D. Bertrand, *Annu. Rev. Pharmacol. Toxicol.* **47**, 699–729 (2007).
35. N. Eshel, J. Tian, M. Bukwich, N. Uchida, *Nat. Neurosci.* **19**, 479–486 (2016).
36. J. G. Parker *et al.*, *Proc. Natl. Acad. Sci. U.S.A.* **107**, 13491–13496 (2010).
37. A. A. Grace, B. S. Bunney, *Science* **210**, 654–656 (1980).
38. L. J. Gentet, S. R. Williams, *J. Neurosci.* **27**, 1892–1901 (2007).
39. N. F. Parker *et al.*, *Nat. Neurosci.* **19**, 845–854 (2016).
40. C. Liu, Data table for an action potential initiation mechanism in distal axons for the control of dopamine release. Zenodo (2022); doi: 10.5281/zenodo.6342359.
41. C. Liu, Matlab script for object recognition and analysis. Zenodo (2022); doi: 10.5281/zenodo.6342367.

ACKNOWLEDGMENTS

We thank C. Qiao, M. Han, and J. Wang for technical assistance; N. Uchida, M. Watabe-Uchida, and I. Tsutsui-Kimura for advice on setting up fiber photometry; A. van den Maagdenberg for Ca$_V$2.1^{floxed} mice and T. Schneider for Ca$_V$2.3^{floxed} mice; and C. Harvey, B. Sabatini, W. Regehr, N. Uchida, J. Williams, and R. Wise for discussions and comments on the manuscript. We acknowledge the Neurobiology Imaging Facility (supported by P30NS072030) and Cell Biology Microscopy Facility for microscope availability and advice. **Funding:** This work was supported by the NIH (R01NS103484 and R01NS083898 to P.S.K. and NINDS Intramural Research Program Grant NS003135 to Z.M.K.), the European Research Council (ERC CoG 865634 to S.H.), the German Research Foundation (DFG; HA6386/10-1 to S.H.), the Dean's Initiative Award for Innovation (to P.S.K.), a Harvard-MIT Joint Research Grant (to P.S.K.), and a Gordon family fellowship (to C.L.). X.C. is a visiting graduate student and received a PhD Mobility National Grants fellowship from Xi'an Jiaotong University/China Scholarship Council. **Author contributions:** Conceptualization: C.L. and P.S.K. Methodology: C.L., X.C., A.R.-J., P.F.K., Z.M.K., S.H., and P.S.K. Investigation: C.L., X.C., A.R.-J., and P.F.K. Resources: Y.L. Visualization: C.L., A.R.-J., P.F.K., and P.S.K. Funding acquisition: P.S.K. Project administration: C.L. and P.S.K. Supervision: C.L. and P.S.K. Writing, original draft: C.L. and P.S.K. Writing, review and editing: C.L., X.C., A.R.-J., P.F.K., Y.L., Z.M.K., S.H., and P.S.K. **Competing interests:** Y.L. is listed as an inventor on a patent application (PCT/CN2018/107533) describing GRAB probes. The other authors declare no competing interests. **Data and material availability**: All data and code are available at Zenodo (*40*, *41*).

SUPPLEMENTARY MATERIALS

science.org/doi/10.1126/science.abn0532
Materials and Methods
Figs. S1 to S11
References (*42*–*48*)
MDAR Reproducibility Checklist
Movies S1 to S2

31 October 2021; accepted 23 February 2022
10.1126/science.abn0532

Science

An action potential initiation mechanism in distal axons for the control of dopamine release

Changliang LiuXintong CaiAndreas Ritzau-JostPaul F. KramerYulong LiZayd M. KhaliqStefan HallermannPascal S. Kaeser

Science, 375 (6587),

Axon firing without signal integration

The standard model of information flow in the nervous system states that neurons receive input through their dendrites and send output through their axons. Liu *et al*. used functional imaging, superresolution microscopy, axonal whole-cell electrophysiology, amperometry, and in vivo photometry to identify a previously unknown form of action potential initiation in dopaminergic axons in the striatum. Unlike the conventional form of action potential initiation near the soma, followed by propagation along the axon to synaptic terminals, in this case, activity starts near the synaptic terminals. Axonal action potentials are promoted by the activation of nicotinic acetylcholine receptors on the dopaminergic axons. —PRS

Science (ISSN) is published by the American Association for the Advancement of Science. 1200 New York Avenue NW, Washington, DC 20005. The title *Science* is a registered trademark of AAAS.

Supplementary Materials for

An action potential initiation mechanism in distal axons for the control of dopamine release

Changliang Liu *et al*.

Corresponding authors: Changliang Liu, changliang_liu@hms.harvard.edu; Pascal S. Kaeser, kaeser@hms.harvard.edu

Science **375**, 1378 (2022)
DOI: 10.1126/science.abn0532

The PDF file includes:

- Materials and Methods
- Figs. S1 to S11
- References

Other Supplementary Material for this manuscript includes the following:

- MDAR Reproducibility Checklist
- Movies S1 to S2

Materials and Methods

Mice

Animal experiments were approved by the Animal Care and Use Committees at Harvard University and at the National Institute of Neurological Disorders and Stroke (NINDS, NIH), and by the federal Saxonian Animal Welfare Committee, Germany, and were in accordance with the European (EU Directive 2010/63/EU, Annex IV for animal experiments) and the Leipzig University Guidelines. Mice were housed with free access to water and food, and males and females were used irrespective of sex in all experiments. Knock-in mice with Cre recombinase expression from the dopamine transporter (DAT) gene locus (denoted as DAT$^{\text{IRES-Cre}}$, RRID: IMSR_JAX:006660) (*42*) and the choline acetyltransferase (ChAT) gene locus (denoted as ChAT$^{\text{IRES-Cre}}$, RRID: IMSR_JAX:006410) (*43*) were used for cell type-specific manipulations of dopamine neurons or ACh neurons, respectively. For labeling vesicles in dopamine neurons or ACh neurons, a reporter line with a CAG promoter-driven loxP-STOP-loxP-synaptophysin-tdTomato cassette in the Rosa26 locus (SYP-tdTomato$^{\text{LSL}}$, RRID: IMSR_JAX:012570) was crossed with DAT$^{\text{IRES-Cre}}$ or ChAT$^{\text{IRES-Cre}}$ mice, respectively. For expression of ChR2 in dopamine neurons or ACh neurons, a knock-in line with a CAG promoter-driven loxP-STOP-loxP-ChR2-EYFP cassette in the Rosa26 locus (ChR2-EYFP$^{\text{LSL}}$, RRID: IMSR_JAX:012569) (*44*) was crossed to DAT$^{\text{IRES-Cre}}$ or ChAT$^{\text{IRES-Cre}}$ mice. For expressing eNpHR3.0 in ACh neurons, a knock-in line containing a CAG promoter-driven loxP-STOP-loxP-eNpHR3.0-EYFP cassette in the Rosa26 locus (eNpHR-EYFP$^{\text{LSL}}$, RRID: IMSR_JAX:014539) (*44*) was crossed with ChAT$^{\text{IRES-Cre}}$ mice. Simultaneous ablation of Ca$_{\text{V}}$2.1 and Ca$_{\text{V}}$2.2 proteins in dopamine neurons was achieved by crossing conditional *Cacna1a* knockout mice (Ca$_{\text{V}}$2.1$^{\text{floxed}}$) (*45*) with conditional *Cacna1b* knockout mice (Ca$_{\text{V}}$2.2$^{\text{floxed}}$, generated from KOMP CSD34514-1a-Wtsi) (*24*) and with DAT$^{\text{IRES-Cre}}$ mice. Deletion of Ca$_{\text{V}}$2.3 in dopamine neurons was achieved by crossing conditional *Cacna1e* knockout mice (Ca$_{\text{V}}$2.3$^{\text{floxed}}$) (*46*) to DAT$^{\text{IRES-Cre}}$ mice. In conditional knockout experiments, cKO$^{\text{DA}}$ mice were mice with homozygous floxed Ca$_{\text{V}}$2 alleles and a heterozygous DAT$^{\text{IRES-Cre}}$ allele. Control mice were siblings of the corresponding cKO$^{\text{DA}}$ mice, with heterozygous floxed Ca_V2 alleles and a heterozygous $DAT^{IRES\text{-}Cre}$ allele.

Stereotaxic surgeries

Unless noted otherwise, surgeries were performed unilaterally and in the right hemisphere. Mice were anesthetized with 5% isoflurane and mounted in a stereotaxic frame. 1.5–2% isoflurane was used to maintain stable anesthesia during surgery. A small hole was drilled after exposing the skull, and the AAVs were injected through a microinjector (108 µm needle diameter) at coordinates described in each individual section with a rate of 0.1 µl/min for a total volume of 1 µl. The microinjector was left in place for 10 min to allow diffusion of the virus after injection. Following recovery from surgery, mice were returned to their home cage for at least 14 days before testing. Viruses were aliquoted, stored at - 80 °C, and diluted immediately before injection. Local lesion of dopamine axons was performed by microinjection of 2 µl 6-OHDA (25 mM in PBS) into the right striatum (coordinates: 1.0 mm anterior from Bregma, 2.0 mm lateral, and 3.3 mm below pia). Specific AAVs used during stereotaxic surgeries are listed below for each experiment.

Slice imaging

Adeno-associated viruses (AAVs) expressing $GRAB_{DA2m}$ (*13*), $rGRAB_{DA1h}$ (*13*), and $GRAB_{ACh3.0}$ (*15*) under a human synapsin 1 (hSyn) promoter (AAV9-hSyn-$GRAB_{DA2m}$, AAV9-hSyn-$rGRAB_{DA1h}$, and AAV9-hSyn-$GRAB_{ACh3.0}$, respectively) were purchased from WZ Biosciences, Inc. with permission from Y.L. For measuring dopamine and ACh release in slices, 1 µl AAV9-hSyn-$GRAB_{DA}$ (3–6 x 10^{12} copies/ml), AAV9-hSyn-$rGRAB_{DA}$ (3–6 x 10^{12} copies/ml), or AAV9-hSyn-$GRAB_{ACh}$ (4–8 x 10^{12} copies/ml) was injected into the midbrain (coordinates relative to Lambda: 1.1 mm anterior, 1.3 mm lateral and 4.2 mm below pia) at 45–77 days of age. 26–43 days after injection, the mice were deeply anesthetized with isoflurane and decapitated. Parasagittal mouse brain slices containing the striatum (250 µm thick unless noted otherwise) were cut using a vibratome (Leica, VT1200s) in an ice-cold cutting solution containing (in mM): 75 NaCl, 2.5 KCl, 7.5 $MgSO_4$, 75 Sucrose, 1 NaH_2PO_4, 12 Glucose, 26.2

$NaHCO_3$, 1 Myo-inositol, 3 Pyruvic acid, 1 Ascorbic acid. After cutting, slices were incubated at room temperature in an incubation solution containing (in mM): 126 NaCl, 2.5 KCl, 2 $CaCl_2$,1.3 $MgSO_4$, 1 NaH_2PO_4, 12 Glucose, 26.2 $NaHCO_3$, 1 Myo-inositol, 3 Pyruvic acid, 1 Ascorbic acid for at least 1 h before use. Recordings were performed in a recording chamber continuously perfused with artificial cerebrospinal fluid (ACSF) containing (in mM): 126 NaCl, 2.5 KCl, 2 $CaCl_2$, 1.3 $MgSO_4$, 1 NaH_2PO_4, 12 Glucose, 26.2 $NaHCO_3$ heated to 30–32 °C at 2.5–3 ml/min. All solutions were constantly bubbled with 95% O_2 and 5% CO_2, and all recordings were completed within 6 h after slicing. Fluorescence imaging was performed using an Olympus BX51 epifluorescence microscope. Fluorescent signals were excited with a 470 or 565 nm LED, collected through a 4X objective, and digitized with a scientific complementary metal-oxide-semiconductor camera (sCMOS, Hamamatsu Orca-Flash4.0). Spontaneous dopamine and ACh release were imaged at 512 x 512 pixels/frame, 10 frames/s, with an exposure time of 50 ms. Evoked responses were acquired at 512 x 512 pixels/frame, 50 frames/s, with an exposure time of 20 ms. Each pixel represents a physical area of 5.4 x 5.4 μm^2. For image analyses, regions of interest (ROIs) containing the striatum were manually selected in each image stack (1–3 min for spontaneous release), and the backgrounds were estimated from cortical regions where no sensor was expressed. After background subtraction, each frame was blurred by box filtering with a radius of 5 pixels. For detection of spontaneous release, a dynamic baseline fluorescence (F_0) was estimated for each pixel by smoothing the time course with a moving average over a 10-s sliding window for 10 times. A time course of $(F-F_0)/F_0$ (from hereon: $\Delta F/F_0$) was then calculated. Image stacks were binarized with a $\Delta F/F_0$ threshold > 0.005 and > 1 x standard deviation (SD) of the $\Delta F/F_0$ of the recording period for each pixel. The pixels above threshold were further filtered with a rise speed of $\Delta F/F_0 > 0.1$ s^{-1} and > 1 x SD of the rise speed for at least 1 frame during the positive periods. Release events were defined as clusters containing more than 20 adjacent pixels above threshold in every frame and more than 500 adjacent pixels above threshold in at least one frame with a total duration of 1.2–6 s for $GRAB_{DA}$ signals and 0.4–2 s for $GRAB_{ACh}$ signals (due to faster kinetics of $GRAB_{ACh}$) (*13*, *15*). Overlapping events were segregated using density-based spatial clustering with a radius of 25% of the raw cluster and a minimum duration of 1 s and 0.3 s for

$GRAB_{DA}$ and $GRAB_{ACh}$, respectively. The segregation process was iterated until no new event was generated. Frequency maps were generated by counting the number of events in each pixel during the recording period. For the quantification of evoked release, F_0 was estimated as the average fluorescence signal over 0.5 s immediately before stimulation. $\Delta F/F_0$ was then calculated for each pixel, and pixels with a $\Delta F/F_0 > 0.02$ in response to electrical stimulation were considered as part of a release event and used for further quantification. Example images in each experiment were contrast adjusted using identical settings. The number of dopamine terminals recruited during a dopamine release event was estimated as the product of the volume of the event (event area x thickness of slice) and the density of synaptophysin-tdTomato-labelled dopamine terminals in the striatum ($0.16/\mu m^3$, SYP-$tdTomato^{LSL}$ x $DAT^{IRES\text{-}Cre}$ mice) (*14*).

Amperometry and field recordings

Carbon-fiber microelectrodes (CFE, 7 µm in diameter, 50–100 mm in length, Goodfellow) were fabricated in the laboratory and calibrated immediately before use by puffing dopamine solutions (*14*). The recording electrode was placed in the dorsal striatal slices prepared as described above, and held at a constant voltage of 600 mV for amperometry. Signals were amplified with a multiclamp 700B amplifier (Molecular Devices), low-pass filtered at 400 Hz, and digitized using a Digidata 1440A Digitizer (Molecular Devices). Electrical stimulation was carried out with a unipolar glass pipette (tip diameter of 3–5 µm) filled with ACSF. The electrode was placed 100–150 µm away from the CFE. The frequency, duration, and magnitude of the stimulus were controlled through a digitizer (1440A) and a linear stimulus isolator (A395, World Precision Instruments). A biphasic wave (0.25 ms in each phase) was applied for stimulation. For the activation of ChR2, brief pulses of light (470 nm; 1 ms duration; 7.5 mW/mm^2) were delivered at the recording site using an LED light source. Recordings in Fig. 2, C to E, were performed after blocking AMPA receptors (CNQX, 20 µM), NMDA receptors (APV, 50 µM), $GABA_A$ receptors (PTX, 50 µM), DAT (CGP55845, 0.1 µM), D2 receptors (sulpiride, 0.6 µM), and muscarinic AChRs (atropine, 2 µM). NpHR3.0 was activated using a 590 nm LED with an output power of 1.8 mW/mm^2.

Evoked field potentials (Fig. 3, A to C) were recorded using the same CFE in current-clamp mode without any current injection and low-pass filtered at 10 kHz. Local lesion of dopamine axons was done as described above, and recordings were performed 16–57 days after the surgery. The extent of the lesion was confirmed post hoc using immunostaining. The recorded slices were fixed with 4% paraformaldehyde (PFA) in PBS for 2 h, blocked in 10% goat serum in PBS, permeabilized in 0.25% Triton X-100 in PBS, stained with rabbit anti-VAChT (1:500, Sysy 139103) and guinea pig anti-TH (1:1,000, RRID: AB_2619897) for 12 h at 4 °C and secondary antibodies (tagged with Alexa 488 and 568) for 2 h at room temperature, mounted on #1.5 cover glasses (GG-18-1.5-pdl, neuVitro) using H-1000 mounting medium (Vectashield), and imaged using an Olympus FV1000 laser scanning confocal microscope.

Patch-clamp electrophysiology

Cell-attached recordings were performed in voltage-clamp mode using acute mouse brain slices prepared with the same method described in slice imaging (postnatal days 51–145). eNpHR3.0-EYFP was expressed in ACh neurons (eNpHR3.0-EYFP^{LSL} mice x ChAT$^{IRES\text{-}Cre}$ mice), and a glass pipette (2–3 µm in diameter) filled with ACSF was used for recording. After a gigaohm seal was established on an eNpHR3.0-EYFP expressing cell, the holding voltage was adjusted until there was no net flow of current through the pipette. Signals were amplified with a Multiclamp 700B amplifier (Molecular Devices), low-pass filtered at 2 kHz, and digitized using a Digidata 1440A Digitizer (Molecular Devices). Action potentials were detected with an amplitude threshold > 3 x SD of the recording and visually inspected afterwards. *Whole-cell axonal recordings* were performed in acute striatal slices from mice (postnatal days 122–181) with the expression of synaptophysin-tdTomato in dopamine neurons (SYP-tdTomato^{LSL} x DAT$^{IRES\text{-}Cre}$). Brain hemispheres mounted in a chamber filled with chilled ACSF were sliced parasagittally at 300 µm and kept in ACSF at 37 °C for 15 minutes. The slices were then transferred to ACSF at room temperature until testing. ACSF for slicing, slice retention and recordings contained (in mM): 125 NaCl, 3 KCl, 25 Glucose, 25 $NaHCO_3$, 1.25 Na_2HPO_4, 1.0 $MgCl_2$, 1.1 $CaCl_2$. For recordings, brain slices were mounted on an upright two-photon laser scanning microscope (Femtonics) equipped with a pulsed Ti:Sapphire laser (MaiTai, SpectraPhysics) tuned to 1020 nm and a 60x/1.0 NA objective (Olympus). Whole-cell current-clamp recordings from dopamine axons in the dorsal striatum were performed with quartz pipettes (Heraeus Quartzglas), pulled by a modified DMZ Universal Electrode Puller with oxygen-hydrogen burner (Zeitz Instruments) to a resistance of 8–17 MΩ. Pipettes were filled with potassium gluconate–based internal solution containing (in mM): 150 K-gluconate, 3 Mg-ATP, 0.3 Na-GTP, 10 K-HEPES, 10 NaCl, and 0.2 EGTA, pH adjusted to 7.2 with KOH. Pipettes were fixed into a custom-built electrode holder mounted on a micromanipulator (Kleindiek Nanotechnik). All recordings were performed in continuously perfused ACSF heated to 34.0–36.5 °C. Membrane voltages were recorded with a Multiclamp 700A patch-clamp amplifier (Molecular Devices) and digitized and filtered (200 kHz and 3 kHz 8-pole Bessel filter, respectively) by a HEKA EPC10/2 amplifier running Patchmaster software (HEKA Elektronik). Pipette capacitances were determined in the cell-attached configuration in voltage-clamp mode by the automated, fast capacitance cancellation of the Multiclamp 700A. Upon establishing whole-cell configuration, the amplifier was changed to current-clamp mode, and pipette capacitance was canceled using the value determined in voltage-clamp as previously established for presynaptic recordings (*26*). Holding currents were adjusted to keep membrane potentials between -70 to -75 mV (not liquid-junction corrected). For stimulation of nAChRs on dopamine axons, a second pipette pulled from borosilicate glass (Science Products, tip opening diameters of 2–3 µm) was used to apply carbachol puffs (100 µM in ACSF with 40–100 µM Atto 488). Puffs (0.6–1.2 bar, 8–30 ms) were applied 20–40 µm away from the recording site at intervals of 10 s. The efflux of carbachol during puff application was inspected by continuous two-photon x-y scans of the fluorescence of Atto 488. The puff-increased Atto 488 fluorescence reached a diameter of 10–15 µm and dissipated within ~2 s. Recorded responses of each axon with action potential firing in response to carbachol puffs are shown (axon 1: Fig. 3J, axons 2 and 3: fig. S7F). For one of the recordings (axon 3), small sinusoidal functions were subtracted from the traces to remove a 50-Hz-electrical noise artifact in this experiment (amplitude 1 to 3 mV, frequency 50 Hz). Irresponsiveness of some axons to carbachol puffs is likely due to suboptimal positioning of the puff pipette relative to nAChRs on dopamine axons. Because the whole-cell recordings from dopamine axons are fragile, limited in time and sensitive to movement of the puff pipette, repositioning of the puff pipette during recordings was not possible. *For perforated patch axonal recordings*, DAT$^{IRES-Cre}$ x ChAT$^{IRES-Cre}$ mice were used. For labeling dopamine axons, AAVs encoding a Cre-dependent double-floxed inverted open reading frame of tdTomato under a CAG promoter (AAV9-CAG-Flex-tdTomato, Penn Vector Core) were injected bilaterally into the substantia nigra (coordinates: 2.4 mm posterior from Bregma, 1.4 mm lateral and 5.2 mm below the skull). For expressing channelrhodopsin in cholinergic interneurons, AAVs encoding a Cre-dependent double-floxed inverted open reading frame of ChR2-EYFP under an Ef1a promoter (AAV5-Ef1a -Flex-ChR2-EYFP, 4 x 10^{12} copies/ml, UNC Vector Core; for 2 mice) or double-floxed inverted open reading frame of channelrhodopsin-GFP under a human synapsin 1 promoter (AAV1-hSyn-Flex-CoChR-GFP, 5.7 x 10^{12} copies/ml, UNC Vector Core; for 1 mouse) were injected bilaterally into the medial dorsal striatum (coordinates: 0.8 mm anterior from Bregma, 1.8 mm lateral and 3.3 mm below the skull). Recordings were performed on adult mice (postnatal days 119–133). Mice were anesthetized with isoflurane, decapitated, and brains were rapidly extracted. Horizontal sections were cut at 330 µm thickness on a vibratome while immersed in heated (34 °C), modified, slicing ACSF containing (in mM): 198 glycerol, 2.5 KCl, 1.2 NaH_2PO_4, 20 HEPES, 25 $NaHCO_3$,10 glucose, 10 $MgCl_2$, 0.5 $CaCl_2$, 5 Na-ascorbate, 3 Na-pyruvate, and 2 thiourea. Cut sections were removed from the slicing chamber and incubated for 30–60 minutes in a heated (34 °C) chamber with holding solution containing (in mM): 92 NaCl, 30 $NaHCO_3$, 1.2 NaH_2PO_4, 2.5 KCl, 35 glucose, 20 HEPES, 2 $MgCl_2$, 2 $CaCl_2$, 5 Na-ascorbate, 3 Na-pyruvate, and 2 thiourea. Slices were then stored at room temperature and used 30 min to 6 h later. Following incubation, slices were moved to a heated (33–35 °C) recording chamber that was continuously perfused with recording ACSF (in mM): 125 NaCl, 25 $NaHCO_3$, 1.25 NaH_2PO_4, 3.5 KCl, 10 glucose, 1 $MgCl_2$, 2 $CaCl_2$. Perforated-patch recordings were made using borosilicate pipettes (5–10 MΩ) filled with an internal solution containing (in mM): 135 KCl, 10 NaCl, 2 $MgCl_2$, 10 HEPES, 0.5 EGTA, 0.1 $CaCl_2$, adjusted to a pH value of 7.43 with KOH, 278 mOsm. Pipette tips were back-filled first with ~1 µl of internal solution lacking gramicidin followed by internal solution containing 80–100 µg/ml gramicidin. Patch integrity was monitored by the addition of Alexa-488 to the gramicidin-containing internal solution. A white light LED (Thorlabs, SOLIS-3C) was used in combination with a tdTomato (Thorlabs, TLV-U-MF2-TOM) or EGFP (Chroma, 49002) filter set to visualize the dopamine axons (tdTomato) or excite the light-activated ion channel (EGFP). For opsin activation, the LED was controlled with a TTL pulse of 2–5 ms.

3D-SIM imaging

3D-SIM imaging was performed following previously described methods (*14*, *47*). Vesicles in ACh neurons were labeled by crossing SYP-tdTomato^{LSL} mice with ChAT$^{IRES\text{-}Cre}$ mice. ChAT$^{IRES\text{-}Cre}$ mice homozygote for SYP-tdTomato^{LSL} were deeply anesthetized with 5% isoflurane at postnatal days 64–75, perfused transcardially with 30 ml PBS at room temperature and 50 ml 4% PFA in PBS at 4 °C. Coronal slices (20 µm thick) containing striatum were cut using a vibratome (Leica, VT1000s) in ice-cold PBS. All slices were blocked in 10% goat serum in PBS, permeabilized in 0.25% Triton X-100 in PBS, stained with rabbit anti-TH (1:1,000, AB152, RRID: AB_390204) antibodies for 12 h at 4 °C and secondary antibodies (tagged with Alexa 488) for 2 h at room temperature, and mounted on #1.5 cover glasses (GG-18-1.5-pdl, neuVitro) using H-1000 mounting medium (Vectashield). 3D-SIM data were acquired with a DeltaVision OMX V4 Blaze microscope (GE Healthcare) equipped with a 60x/1.42 N.A. oil immersion objective and separate Edge 5.5 sCMOS cameras (PCO) for each channel. Z stacks were acquired with a z-step of 125 nm and 15 raw images per plane (five phases, three angles). Spherical aberrations were minimized using immersion oil matching. Superresolution images were computationally reconstructed from the raw datasets with a channel-specific measured optical transfer function and a Wiener filter constant of 0.002–0.003. Channel misregistration was measured using a control slide, and multi-channel datasets were registered. 3–5 ROIs were imaged from the dorsal striatum in each slice with imaging volumes of 40 x 40 x 2.5 µm^3. For analyses, ROIs (21.7 x 20.7 x 1 µm^3 – 36.3.7 x 37.4 x 2 µm^3) with a relatively even distribution of labeled terminals were manually selected in each image stack, and a custom MATLAB program described before (*14, 41*) was used to analyze the 3D datasets. Binary images in each layer of the stack were first generated with the threshold determined by automatic two-dimensional segmentation (Otsu algorithm). Objects in each channel were recognized by the size of the cluster formed by contiguous voxels with a size filter of 0.04–2 μm^3. The minimal distance of each cholinergic nerve terminal from the nearest TH axon surface was calculated, and terminals with an overlap of > 0 voxels were considered contacting. Shuffled data were generated by randomly relocating cholinergic terminals within 5 x 5 x 1 μm^3. The effect of shuffling was evaluated by averaging 1,000 rounds of shuffling and distance quantification. Volume and surface rendering of the example images were generated from raw images stacks using Imaris (BITPLANE) with contrast adjusted using identical settings for all images.

In vivo fiber photometry

AAV9-hSyn-GRAB$_{DA2m}$ (2–3 x 10^{12} copies/ml) and AAV9-CAG-tdTomato (1–2 x 10^{12} copies/ml), or AAV9-hSyn-GRAB$_{ACh3.0}$ (2–3 x 10^{12} copies/ml) and AAV9-CAG-tdTomato (1–2 x 10^{12} copies/ml), or AAV9-hSyn-GRAB$_{ACh3.0}$ (2–3 x 10^{12} copies/ml) and AAV9-hSyn-rGRAB$_{DA1h}$ (2–3 x 10^{12} copies/ml) were co-injected into the right dorsal striatum (coordinates: 0.5 mm anterior from Bregma, 1.8 mm lateral and 2.2 mm below pia) of 50–92 day old mice. An optofluid cannula (400 μm in diameter, Doric) was implanted at the same location immediately after virus injection. The cannula was fixed on the skull using dental cement and two bone screws (1.17 mm in diameter, Fine Science Tools). Animals were kept in an inverted 12/12-h light/dark cycle, and experiments were carried out 18–43 days after the surgery during the dark phase of the cycle. The mouse was connected to a fiber optic (400 μm in diameter, Doric) and a drug delivery tube and placed in a round arena (43 cm in diameter) illuminated with infrared light (850 nm, 30 μW/cm^2). Fiber photometric recordings started 5 min after the mice were placed in the arena and lasted for 60 min for each session using a custom-built system. Photometry signals were converted by silicon photodiodes (SM1PD1A, Thorlabs), amplified by photodiode amplifiers (PDA200C, Thorlabs), and sampled at 10,000 Hz by a multifunction I/O card (PCIe-6321, National Instruments). 470 nm and 565 nm LEDs (Thorlabs) were alternatively turned on for 10 ms every 40 ms (25 Hz), and the output in each channel during each cycle was assessed by averaging the readout when the corresponding LED was on. The light power at the fiber end was adjusted (40–160 μW for 470 nm and 10–60 μW for 565 nm) at the beginning of each experiment to keep the signal of the two channels at similar levels. Animal behavior was recorded using an sCMOS camera (Thorlabs) synchronized with fiber photometry acquisition through a TTL control at 25 frames/s. Sensory stimuli were carried out by light flashes (565 nm LED, 50 μW/cm^2) that illuminated the open field arena for 200 ms at random intervals of 100-600 s. Synchrony of image acquisition and photometry was calibrated and confirmed using light flashes. Drugs were locally delivered using a microinjection syringe pump (Harvard Apparatus) at a rate of 0.1 μl/min for a total volume of 1 μl. Half of the tested animals were treated with ACSF (in mM, 155 NaCl, 2.5 KCl, 1.2 $CaCl_2$, 1.2 $MgCl_2$, and 5 glucose) on the first day of the test and DHβE (50–100 μM in ACSF, Tocris) in the following test carried out 24–48 h after. The other half were treated with DHβE first and ACSF later. Haloperidol (2 mg/kg) was injected intraperitoneally in tests performed at least 24 h after completing the local drug infusion experiments. For analyses, F_0 was first estimated by low-pass filtering of the raw data at 0.01 Hz, and $\Delta F/F_0$ was then calculated. For behavioral analyses, the snout, ears, and tail base were tracked in the videos using DeepLabCut (50-layer ResNet-50) trained with 840 distinct frames extracted from multiple videos for 1.02 million training iterations (*48*). Only video frames with tracking confidence levels > 0.99 were included in further analyses, and frames 1 s before and 10 s after the light flashes were excluded from the analysis. Head orientation was determined by the direction from the middle point of the two ears to the snout. Snout velocity at time point t was calculated from the snout displacement between t - 1 and t + 1 frames. The relative angle of velocity and head orientation was then calculated for each time point. For assessing the relationships between photometry signals and behavior, velocities whose amplitude and angle appeared less than 4 times during a 60-min recording session were considered rare events and excluded from the analyses. Movement initiations were defined as transitions from a low mobility state (velocity amplitude < 2 x SD and 25 mm/s for at least 1 s) to a high mobility state (velocity amplitude > 2 x SD and 25 mm/s for at least 80 ms). For comparison of movement initiation in response to local drug infusion, the threshold was reduced to include low-amplitude movement initiations as transitions from velocity amplitude < 0.5 x SD and 25 mm/s for at least 400 ms to velocity amplitude >

0.5 x SD and 25 mm/s for at least 80 ms. $GRAB_{DA}$ transients during movement were defined as transients during which the amplitude of the snout velocity was above the average speed of the recording period and 25 mm/s. $GRAB_{DA}$ transients at rest were defined as transients during which the amplitude of the velocity was lower than mean – 0.2 x SD and 10 mm/s. For quantification of initiation time of $GRAB_{ACh}$ and $rGRAB_{DA}$ to light stimulation, responses that exhibited an increase of z-score > 0.5 within 200 ms following the start of light stimulation in both channels were selected. The initiation time was defined as the time point of the fastest increase in the signals within 400 ms immediately after the start of stimulation.

Statistics

Data are shown as mean ± SEM unless noted otherwise. Numbers of observations in each experiment were based on previous publications and on trial experiments. No statistical methods were used to predetermine sample sizes. The experimenter was blind to genotype while acquiring and analyzing data in Fig. 2, F to I, and fig. S5, C and D, and blind to the drug treatment condition during data analysis in Fig. 4, G to M, and fig. S11. Statistical significance was set at * $p < 0.05$, ** $p < 0.01$, and *** $p < 0.001$. For each experiment, the values and definitions of n are specified in the figure legends. Mann-Whitney rank-sum tests were used for Figs. 1H, 2I, 3M, 4D, 4F, 4K and 4L; figs S1F, S1G, S2A, S2B, S4F, S4J, S4L, S4N, S10C, S10F, S11D, S11E, and S11H. Wilcoxon signed-rank tests were used for Figs. 1E, 1G, 1K, 1L, 1O, 1P, 2E, and 4H; figs. S2, C to H, S3G, S4C, S4D, S4G, S4H, S8C, S11B, S11F, S11G, and S11I. Kruskal-Wallis analysis of variance with post hoc Dunn's tests were used for multigroup comparisons in Fig. 3F; figs. S1D, S1E, and S3D. Two-way ANOVA tests were performed for Fig. 2G, figs. S5D and S7E; a Kolmogorov-Smirnov test was used for Fig. 2B.

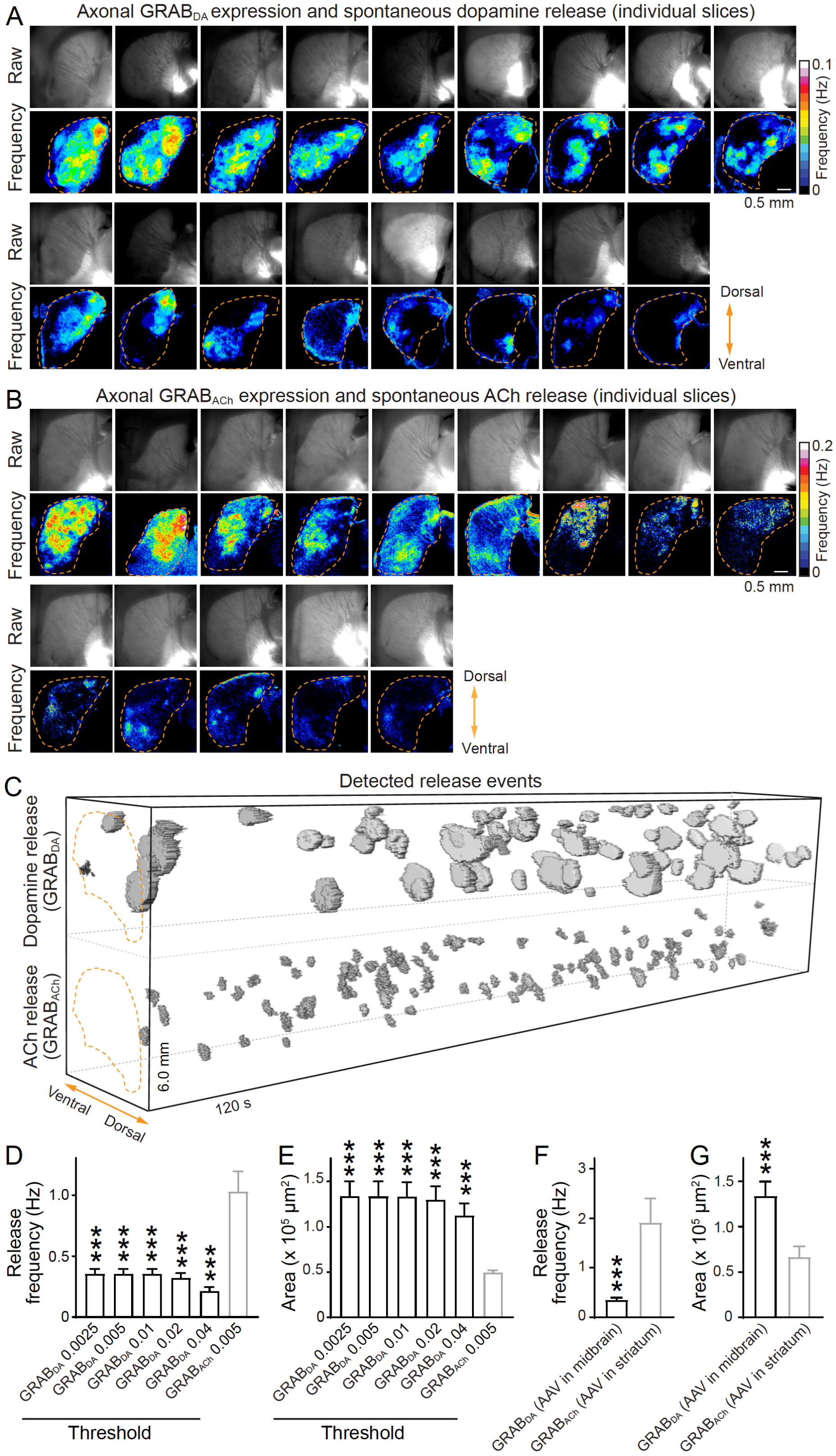

Fig. S1. Dopamine and ACh release measurements with fluorescent sensors. (**A**) Overview of

$GRAB_{DA}$ expression (top) and frequency map of spontaneous dopamine release (bottom) of each individual striatal slice of the experiment shown in Fig. 1, D and E. Dashed lines outline the striatum. Spontaneous dopamine release occurs in both the dorsal and ventral striatum and inhomogeneity in sensor expression does not explain the release patterns revealed by $GRAB_{DA}$ fluorescence changes. (**B**) As (A), but for spontaneous ACh release imaged via $GRAB_{ACh}$. (**C**) Volume-rendered dopamine (top) and ACh (bottom) release events detected via thresholding of fluorescence changes of $GRAB_{DA}$ and $GRAB_{ACh}$, respectively. Dopamine release appears less frequent but invades a larger area than ACh release. Experiments were done in different mice (expressing either $GRAB_{DA}$ or $GRAB_{ACh}$). (**D, E**) Quantification of frequency (D) and area (E) of release events detected with increasing thresholds for $GRAB_{DA}$ changes. Varying $GRAB_{DA}$ detection thresholds did not change the observations of lower frequency and larger area of $GRAB_{DA}$ events compared to $GRAB_{ACh}$ events; n = 17 slices/4 mice for $GRAB_{DA}$, 14/4 for $GRAB_{ACh}$. Original data identical to the data shown in Fig. 1, D to H, the threshold used for the experiments shown in Fig. 1, D to H, was 0.005 for both $GRAB_{DA}$ and $GRAB_{ACh}$. (**F, G**) Comparison of frequency (D) and area (E) of $GRAB_{DA}$ and $GRAB_{ACh}$ events in an experiment in which AAV-hSyn-$GRAB_{ACh}$ was injected into the striatum instead of the midbrain. Striatal $GRAB_{ACh}$ expression increased the frequency of detected events, but the $GRAB_{ACh}$ event area was still smaller than that of $GRAB_{DA}$. $GRAB_{DA}$ data are replotted from E with a threshold of 0.005; n = 17/4 for $GRAB_{DA}$, 8/3 for $GRAB_{ACh.}$ Data are mean ± SEM; *** $p < 0.001$; Kruskal-Wallis analysis of variance with post hoc Dunn's tests for (D) and (E); Mann-Whitney rank-sum tests for (F) and (G).

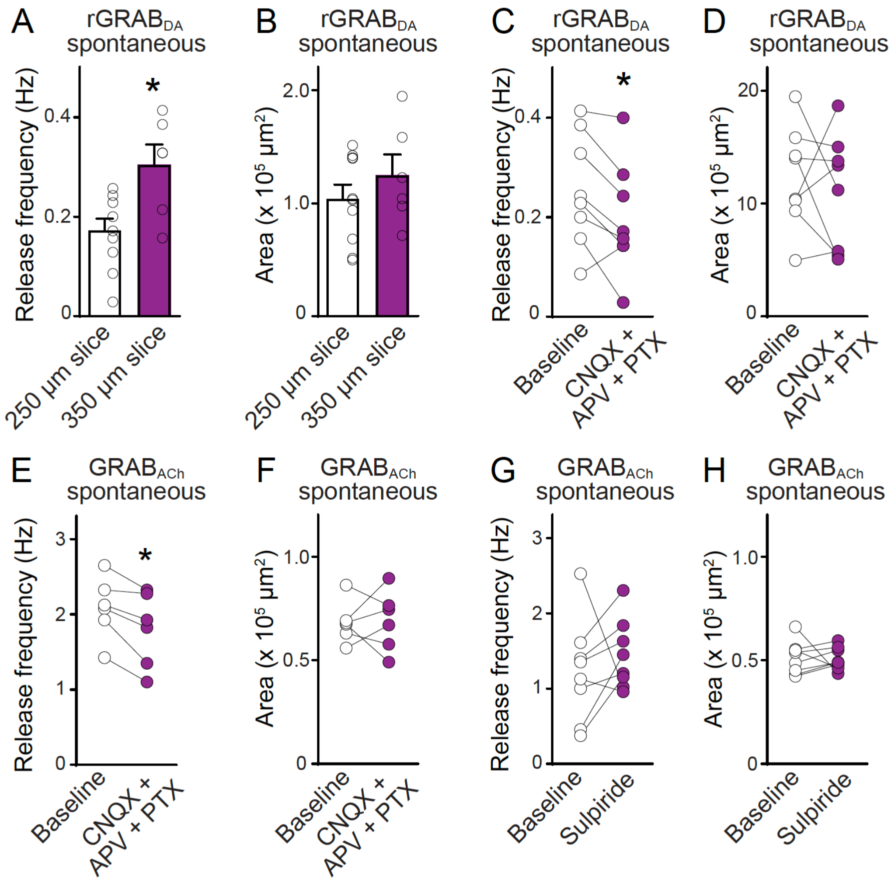

Fig. S2. Additional characteristics of spontaneous dopamine and ACh release. (**A, B**) Comparison of frequency (A) and area (B) of spontaneous dopamine release events detected using rGRAB$_{DA}$ in 250 or 350 µm thick slices. Higher frequency was detected in thicker slices; n = 10 slices/5 mice (250 µm), 6/5 (350 µm). (**C, D**) Quantification of frequency (C) and area (D) of dopamine release events before and after blocking AMPA receptors (CNQX, 20 µM), NMDA receptors (APV, 50 µM), and GABA$_A$ receptors (PTX, 50 µM); n = 8/3. (**E, F**) As (C, D), but for ACh release detected via GRAB$_{ACh}$; n = 6/3. (**G, H**) As (E, F), but before and after blocking D2 receptors with 0.6 µM sulpiride; n = 8/3. The increased frequency of GRAB$_{DA}$ events in thicker slices and relative insensitivity to blockers of synaptic transmission suggest that the spontaneous dopamine release is most likely caused by coincidence of pacemaker firing of cholinergic interneurons. Data are mean ± SEM; * $p < 0.05$; Mann-Whitney rank-sum tests for (A) and (B); Wilcoxon signed-rank tests for (C) to (H).

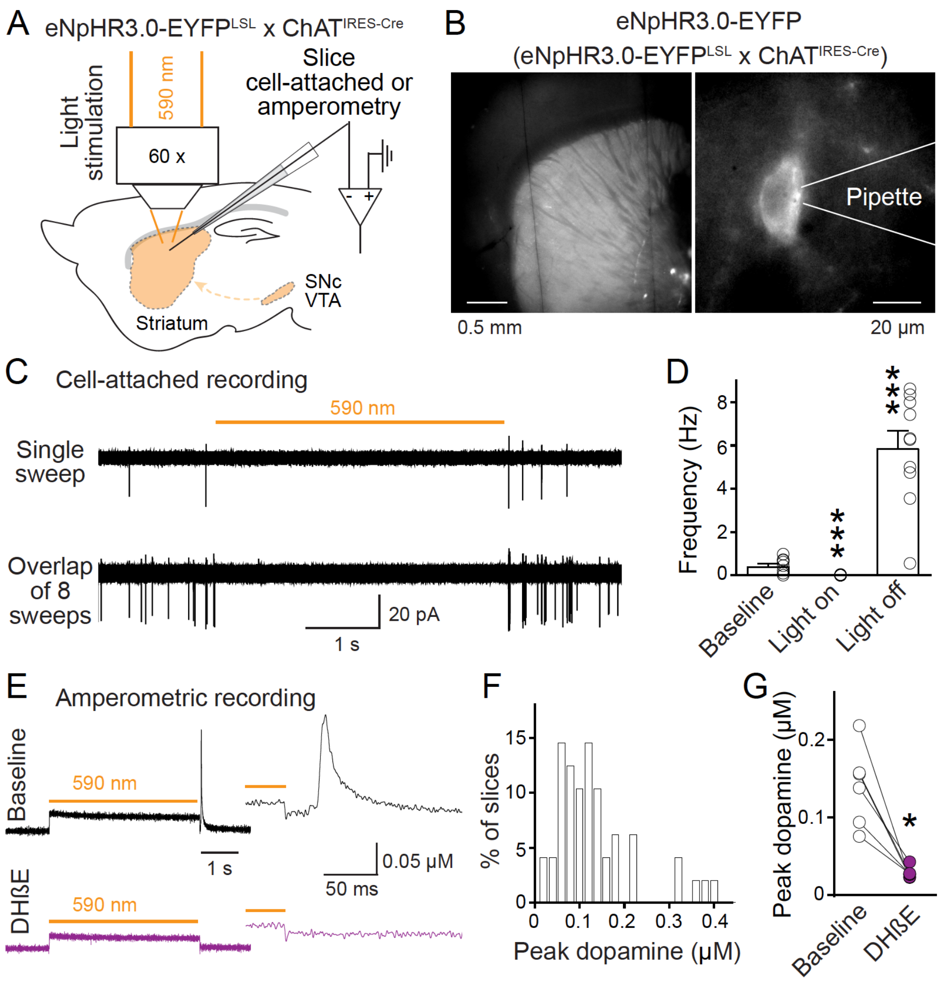

Fig. S3. Pause-rebound activity of ACh neurons induces dopamine release. (**A**) Strategy for mimicking the pause-rebound activity of ACh neurons. eNpHR3.0 was expressed using mouse genetics in ACh neurons. A 590 nm light pulse was used for silencing the firing of ACh neurons, and cell-attached recordings from ACh neurons or amperometry for dopamine were performed. (**B**) Example images of eNpHR3.0-EYFP expression in the striatum (left) and cell-attached recording from an ACh neuron (right). (**C**) Example traces of cell-attached recording of an ACh neuron in response to 4-s 590 nm LED light pulses. The light pulse suppressed spontaneous ACh neuron firing, and turning off this inhibition induced transient activity. (**D**) Quantification of firing frequencies before, during, and immediately after (0–200 ms) the light pulses; n = 10 cells/5 mice. (**E to G**) Example traces (E) and quantification (F and G) of amperometric recordings of dopamine release during the pause-rebound experiment, before and after blocking nAChRs with 1 μM DHβE. Immediately after relieving the light-mediated inhibition, DHβE-sensitive dopamine transients were detected. (F) shows the frequency distribution of the peak of dopamine transients 0–200 ms after the light pulse, and (G) shows peak dopamine levels; F, n = 48 slices/7 mice; G, n = 6/4. Data are mean ± SEM; *** $p < 0.001$, * $p < 0.05$; Kruskal-Wallis analysis of variance with post hoc Dunn's test for (D); Wilcoxon signed-rank test for (G).

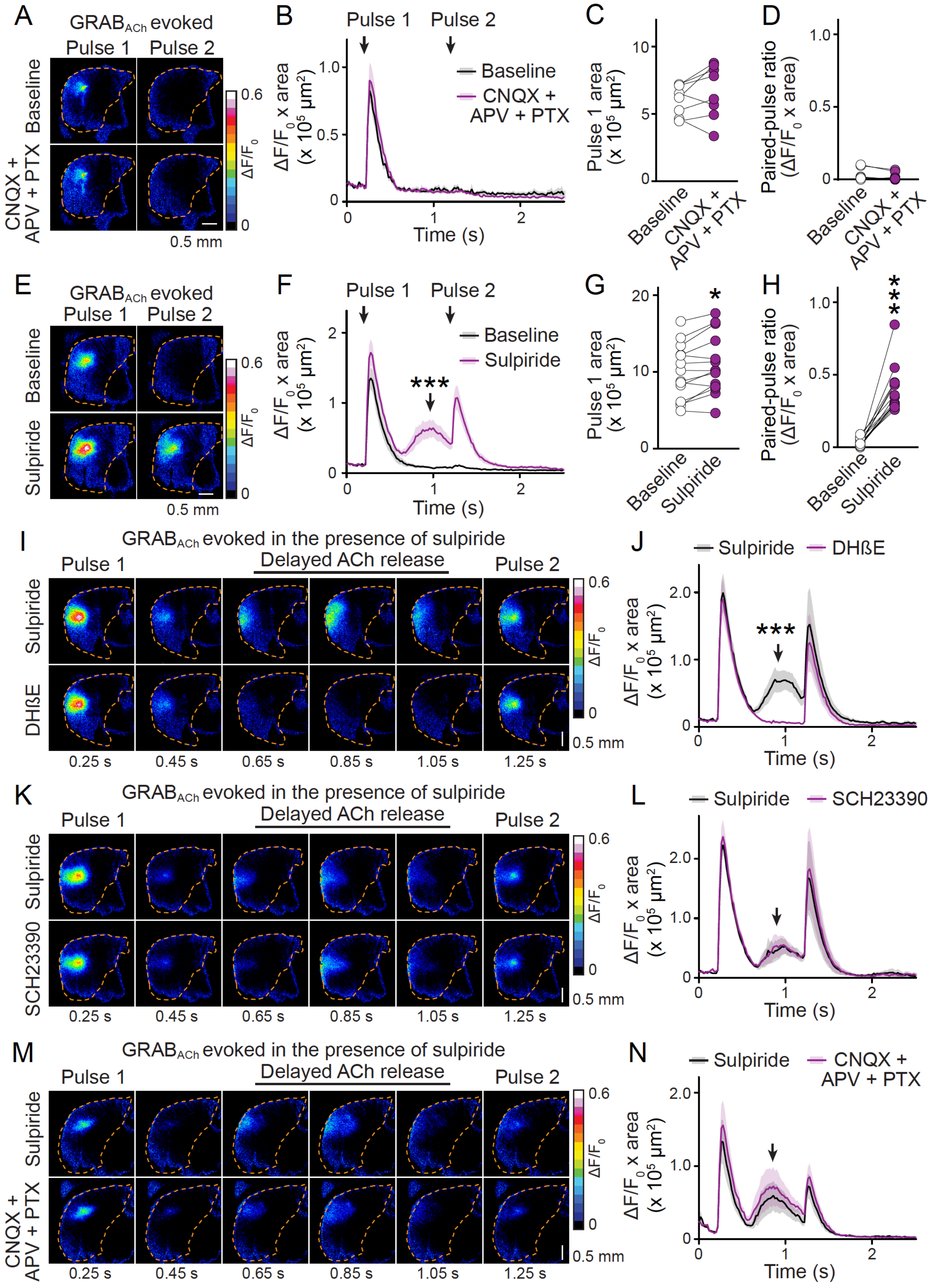

Fig. S4. D2 receptor-mediated feedback inhibition of ACh release. (**A to D**) Example images (A) and quantification (B to D) of GRAB_{ACh} signals evoked by paired electrical stimuli with an interval of 1 s before and after the blockade of AMPA receptors (CNQX, 20 µM), NMDA receptors (APV, 50 µM), and GABA_{A} receptors (PTX, 50 µM). No significant change was detected; n = 8 slices/3 mice. (**E to H**) Similar to A to D, but showing the effects of blocking D2 receptors with 0.6 µM sulpiride. D2 inhibition enhanced GRAB_{ACh} signals to both stimuli and induced an additional delayed phase (black arrow) of ACh release in response to the first stimulus that peaked at ~600–800 ms after stimulation; n = 14/4. (**I, J**) Example images (I) and quantification (J) of the additional delayed ACh release in the presence of 0.6 µM sulpiride before and after blockade of nAChRs with 1 µM DHβE. The delayed ACh release was abolished by DHβE, suggesting that it is caused by feedback mechanisms that involve nAChRs; n = 8/3. (**K to N**) As (I, J), but for blockade of D1 receptors with 1 µM SCH23390 (K, L) or AMPA receptors with 20 µM CNQX, NMDA receptors with 50 µM APV, and GABA_{A} receptors with 50 µM PTX (M, N). No significant change in the delayed ACh release was seen; n = 6/3 each. Data are mean ± SEM; *** $p < 0.001$, * $p < 0.05$; Wilcoxon signed-rank tests for (C), (D), (G), and (H); Mann-Whitney rank-sum tests for areas under the curve (600–1200 ms) in (F), (J), (L), and (N).

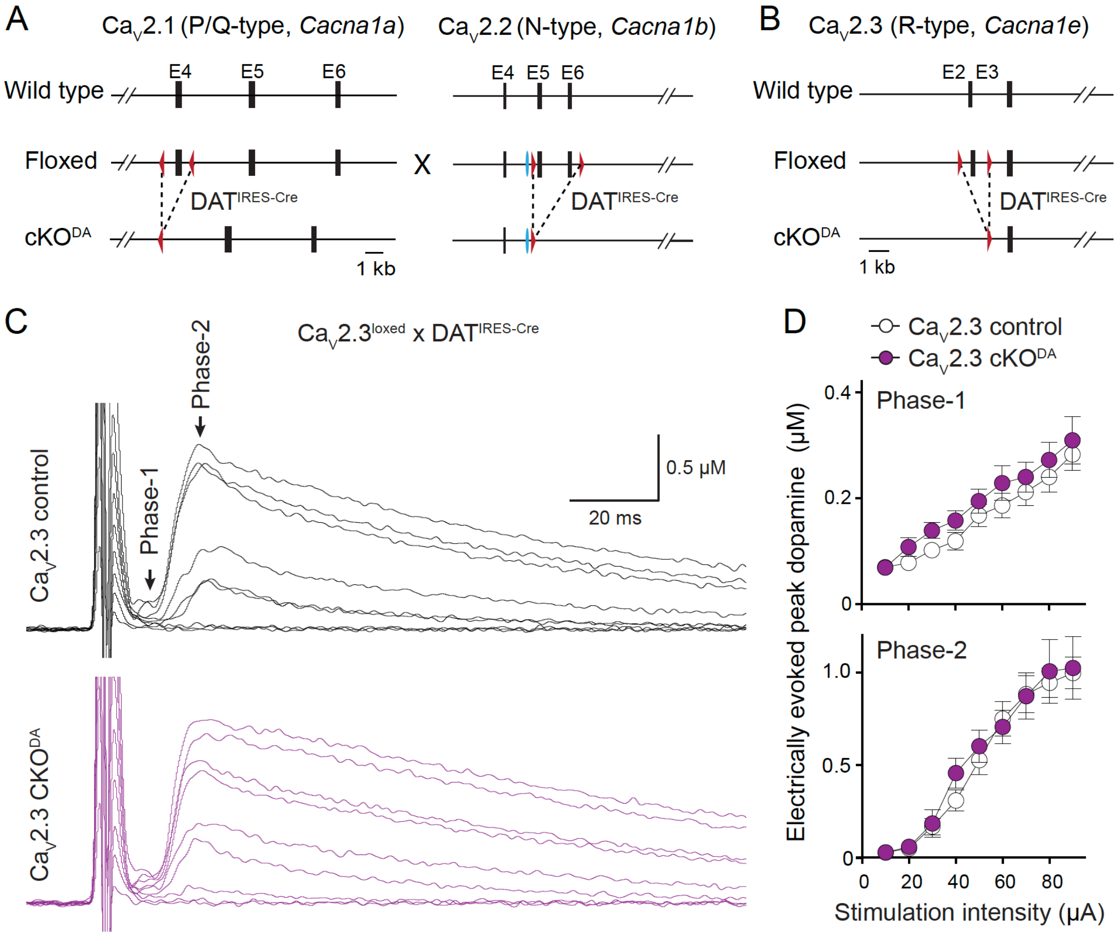

Fig. S5. Strategies for Ca_V2 ablation from dopamine neurons, and assessment of roles of $Ca_V2.3$ in dopamine release. (**A**) Simultaneous ablation of $Ca_V2.1$ and $Ca_V2.2$ from dopamine neurons by crossing conditional *Cacna1a* ($Ca_V2.1^{floxed}$) and *Cacna1b* ($Ca_V2.2^{floxed}$) knockout mice with $DAT^{IRES-Cre}$ mice. (**B**) Ablation of $Ca_V2.3$ from dopamine neurons by crossing conditional *Cacna1e* mice ($Ca_V2.3^{floxed}$) to $DAT^{IRES-Cre}$ mice. (**C, D**) Example traces (C) and quantification of peak amplitudes (D) of dopamine release evoked by electrical stimulation in mice in which $Ca_V2.3$ was ablated in dopamine neurons ($Ca_V2.3$ cKO^{DA}) and sibling control mice ($Ca_V2.3$ control). Phase-1 dopamine release was measured as the peak response within 10 ms after the stimulation, and phase-2 dopamine release was assessed as additional release after phase-1; n = 12 slices/4 mice for $Ca_V2.3$ control, 10/4 for $Ca_V2.3$ cKO^{DA}. $p > 0.05$ for genotype, stimulation intensity and interaction; two-way ANOVA. Data are mean ± SEM.

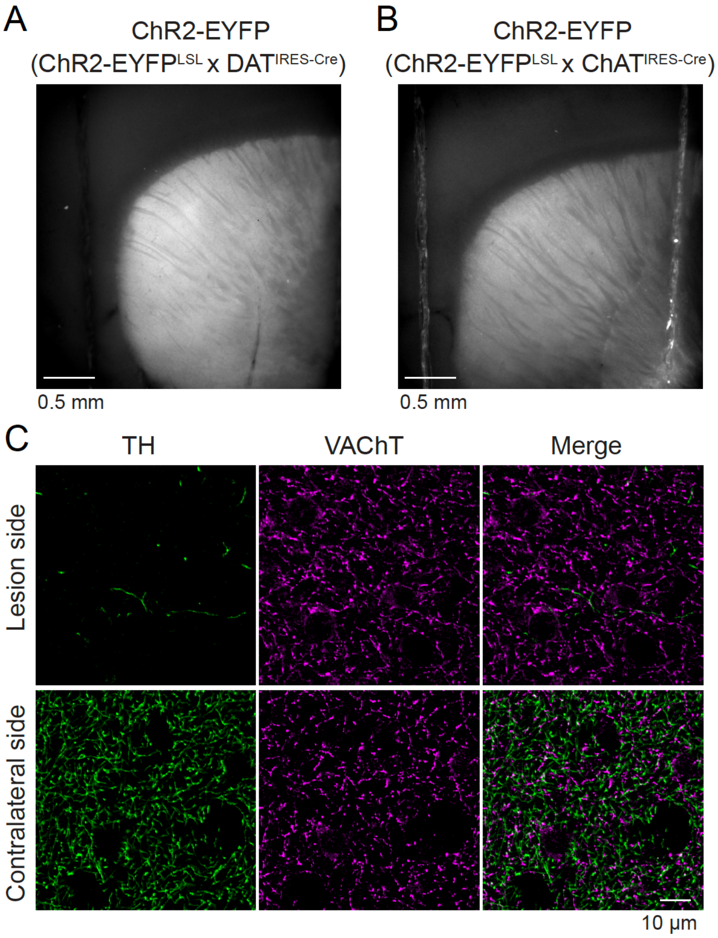

Fig. S6. ChR2-EYFP expression and 6-OHDA lesions. (**A, B**) Example images of sagittal striatal slices showing the distribution of ChR2-EYFP expressed in dopamine axons (A, crossing ChR2-EYFP^{LSL} mice to DAT$^{IRES\text{-}Cre}$ mice) and ACh neurons (B, crossing ChR2-EYFP^{LSL} mice to ChAT$^{IRES\text{-}Cre}$ mice). (**C**) Example confocal images of coronal striatal slices of TH and VAChT antibody staining in the lesioned and control sides of a mouse after unilateral 6-OHDA injection into the striatum. 6-OHDA lesion resulted in a loss of dopamine axons at the injection site but left cholinergic terminals intact.

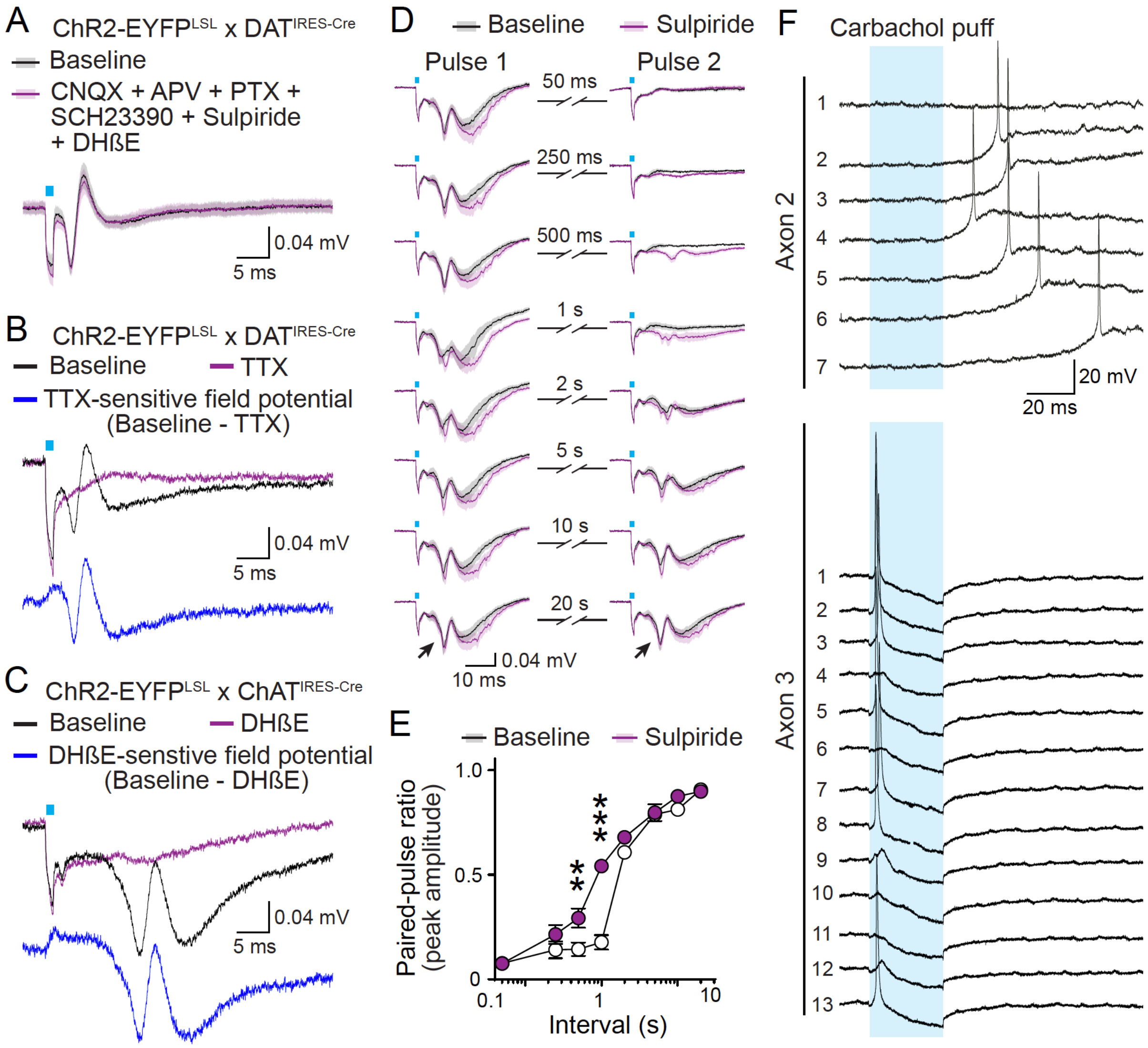

Fig. S7. Additional analyses of ACh-induced field potentials and carbachol-induced action potentials. (**A**) Average traces of light-evoked field potentials in mice expressing ChR2-EYFP in dopamine neurons, before and after the blockade of AMPA receptors (CNQX, 20 μM), NMDA receptors (APV, 50 μM), GABA$_A$ receptors (PTX, 50 μM), D1 receptors (SCH23390, 1 μM), D2 receptors (Sulpiride, 0.6 μM), and nAChRs (DHβE, 1 μM); n = 5 slices/1 mouse. (**B**) Example traces of field potential recordings (average of 4 sweeps from a single slice) before and after the application of 1 μM TTX, mice used in this experiment express ChR2-EYFP in dopamine axons. The TTX-sensitive field potential was obtained by subtracting the leftover signal in the presence of TTX from the baseline. (**C**) As (B), but for application of 1 μM DHβE in mice that express ChR2-EYFP in ACh neurons. (**D**) Average traces of field potentials in response to paired-pulse stimulation using light (blue bar) with increasing interstimulus intervals before and after blocking D2 receptors with 0.6 µM sulpiride in mice expressing ChR2-EYFP in ACh neurons; n = 8/3. (**E**) Quantification of the paired-pulse ratios of the peak potential 5–15 ms after stimulation, arrows in bottom traces in (D). D2 receptor blockade significantly increased the amplitude of field potentials in response to the second stimulus when intervals were shorter than 2 s. These data indicate that the full depression of ACh-induced dopamine release during repetitive stimulation (Fig. 1, I to L) is caused mainly by dopamine feedback that reduces the capacity of ACh to induce firing in dopamine axons; n = 8/3; $p < 0.001$ for treatment, stimulation interval, and interaction; two-way ANOVA with post hoc Bonferroni test. (**F**) Example responses of dopamine axons 2 and 3 (axon 1 is shown in Fig. 3J) to carbachol puffs (100 µM, 10-s intervals). Carbachol puffing induced action potential firing in 3 of 14 recorded axons, likely because in many cases the positioning of the carbachol puff pipette was too distant from axonal nAChRs. The apparent hyperpolarization that follows the action potential in axon 3 is most likely an artifact caused by the puff or other mechanical movement. The variable delay in response to puffs is not dominated by action potential conduction velocities, but instead likely related to the positioning of the puff pipette, the opening of nAChRs, and charging and depolarizing the dopamine axonal membrane before action potential induction in dopamine axons. Similarly, in the optogenetic activation experiment shown in Fig. 3L, the ~10-ms delay is mainly due to the time it takes to sufficiently depolarize the axonal membrane. Data are mean ± SEM. *** $p < 0.001$, ** $p < 0.01$.

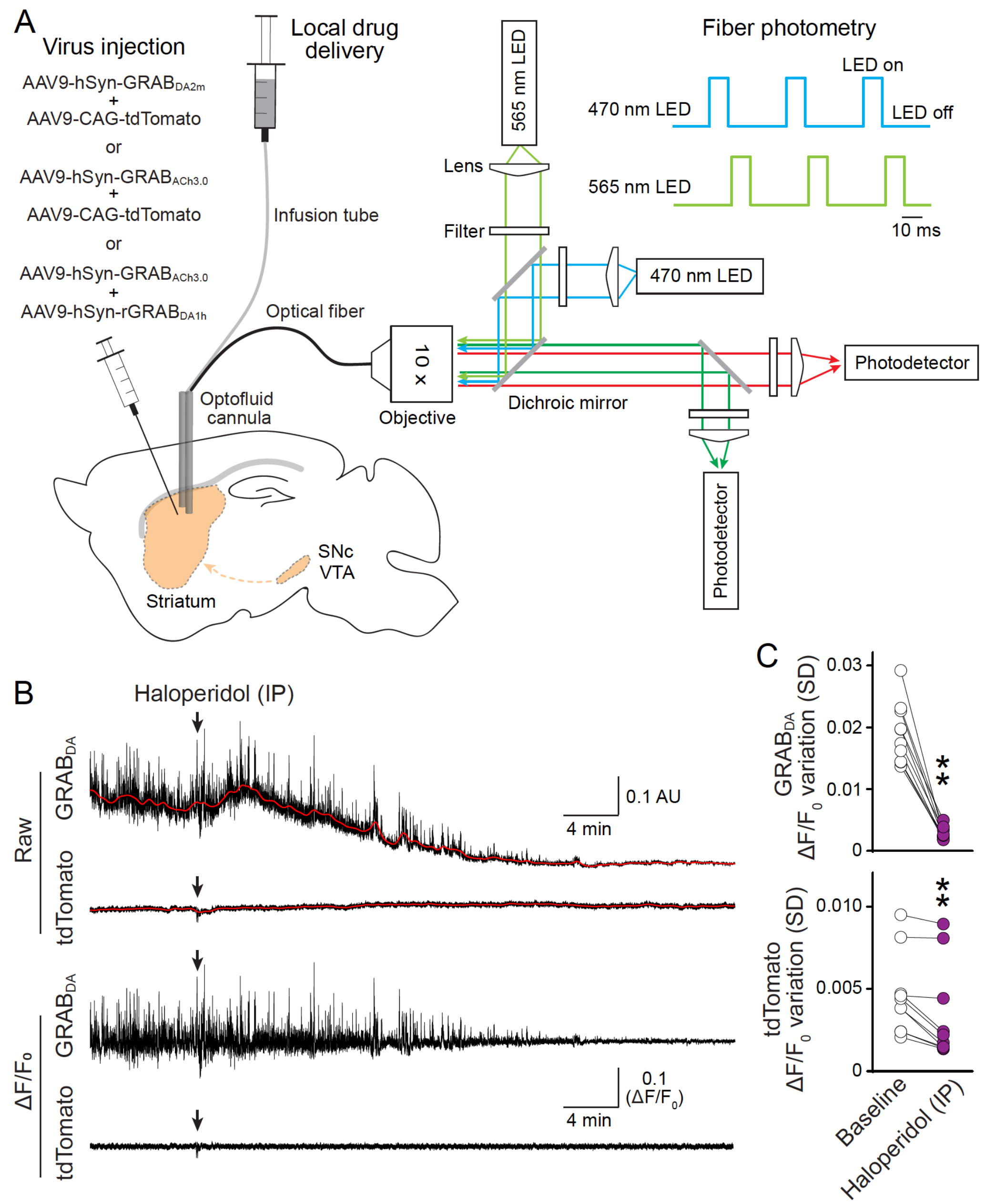

Fig. S8. Fiber photometry and drug delivery. (**A**) Schematic of AAV injection, photometry, and local drug delivery. AAVs were injected, and an optofluid cannula was implanted in the dorsal striatum of the right hemisphere in the same surgery. Photometry signals were acquired at 25 Hz with alternating illumination with 470-nm and 565-nm LEDs for 10 ms each in every 40-ms cycle. GRAB$_{DA}$ or GRAB$_{ACh}$ signals were only acquired when 470-nm LED was on, and the tdTomato or rGRAB$_{DA}$ signals were only acquired when the 565-nm LED was on. Local application of DHβE (50–100 μM) and ACSF were carried out using a microinjection pump at a speed of 0.1 µl/min for 10 min. (**B**) Example recordings (top) and $\Delta F/F_0$ (bottom) of GRAB_{DA} and tdTomato signals before and after intraperitoneal injection of the D2 receptor antagonist haloperidol (2 mg/kg, arrows). F_0 was estimated by low-pass filtering of the raw data at 0.01 Hz (red line). (**C**) Quantification of GRAB_{DA} and tdTomato fluctuations (standard deviation of $\Delta F/F_0$) before and after intraperitoneal (IP) injection of haloperidol (2 mg/kg, arrows). Haloperidol abolished GRAB_{DA} fluctuations. There is also a small but significant reduction in tdTomato fluctuations, most likely due to photobleaching and reduced movement in response to haloperidol; n = 10 mice. Data are mean ± SEM; ** $p < 0.01$; Wilcoxon signed-rank test for (C).

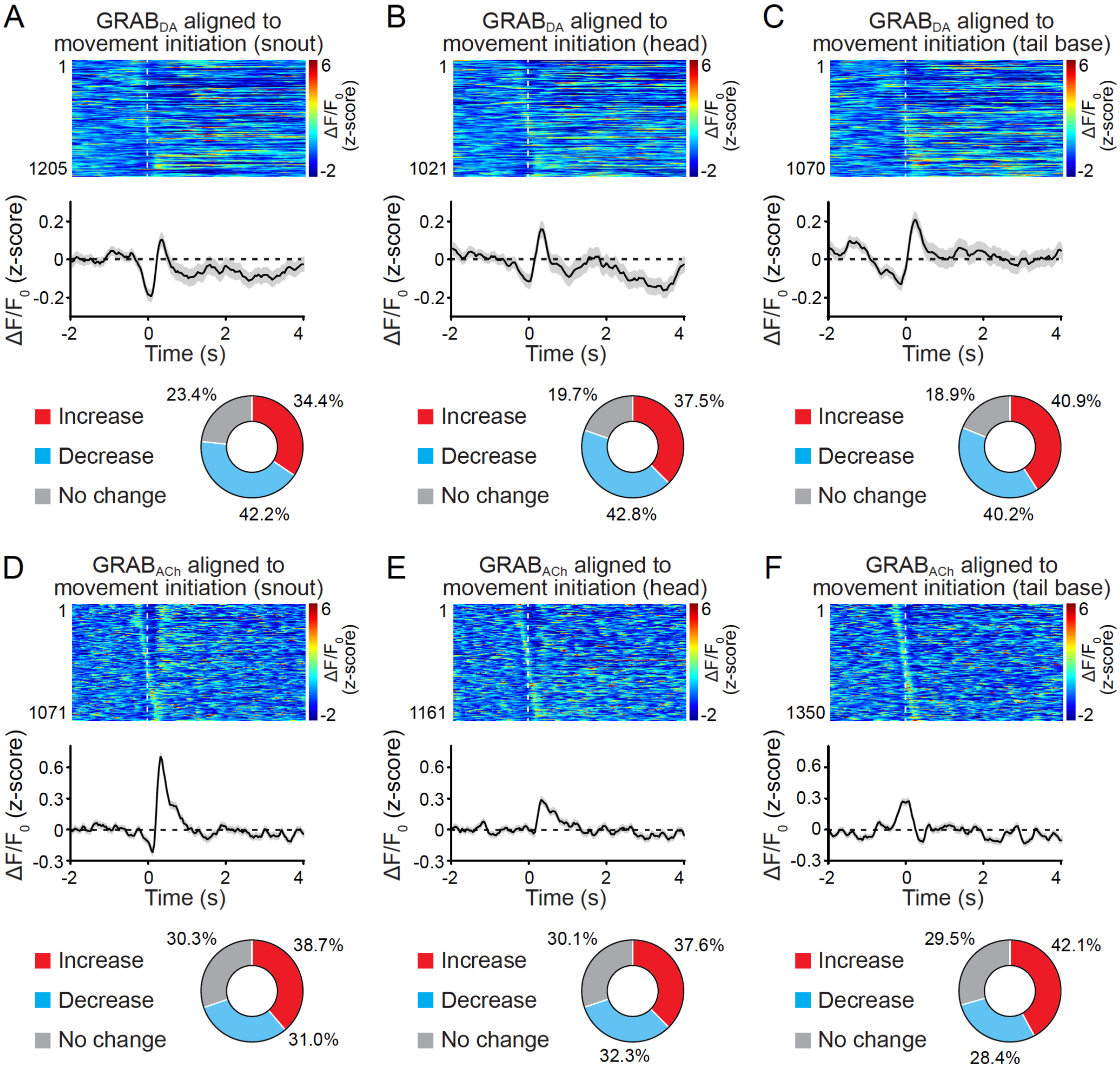

Fig. S9. Heterogeneity in GRAB$_{DA}$ and GRAB$_{ACh}$ dynamics during movement initiation. (**A to C**) Individual (top, heatmap, sorted by peak time), average (middle), and grouped (bottom) GRAB$_{DA}$ signals aligned to movement initiation (dashed line) based on the snout (A), the head (B, the center point between snout and ears), or the tail base (C). A response was considered an increase or a decrease when the z-score of the fluorescence change, assessed by the area ranging from 400 ms before to 400 ms after the movement initiation, was above 0.2 or below - 0.2, respectively. GRAB$_{DA}$ signals exhibit strong heterogeneity during movement initiation regardless of the body part used for movement analysis, illustrating that other factors or uncharacterized dimensions of movement contribute to striatal dopamine and ACh dynamics; A, n = 1205 events/10 mice; B, 1021/10, C, 1070/10 (C). (**D to F**) As A to C, but for

GRAB_{ACh}. Heterogeneity also exists in GRAB_{ACh} signals during movement initiation; D, n = 1071/11; E, 1161/11; F, 1350/11. Data are mean ± SEM.

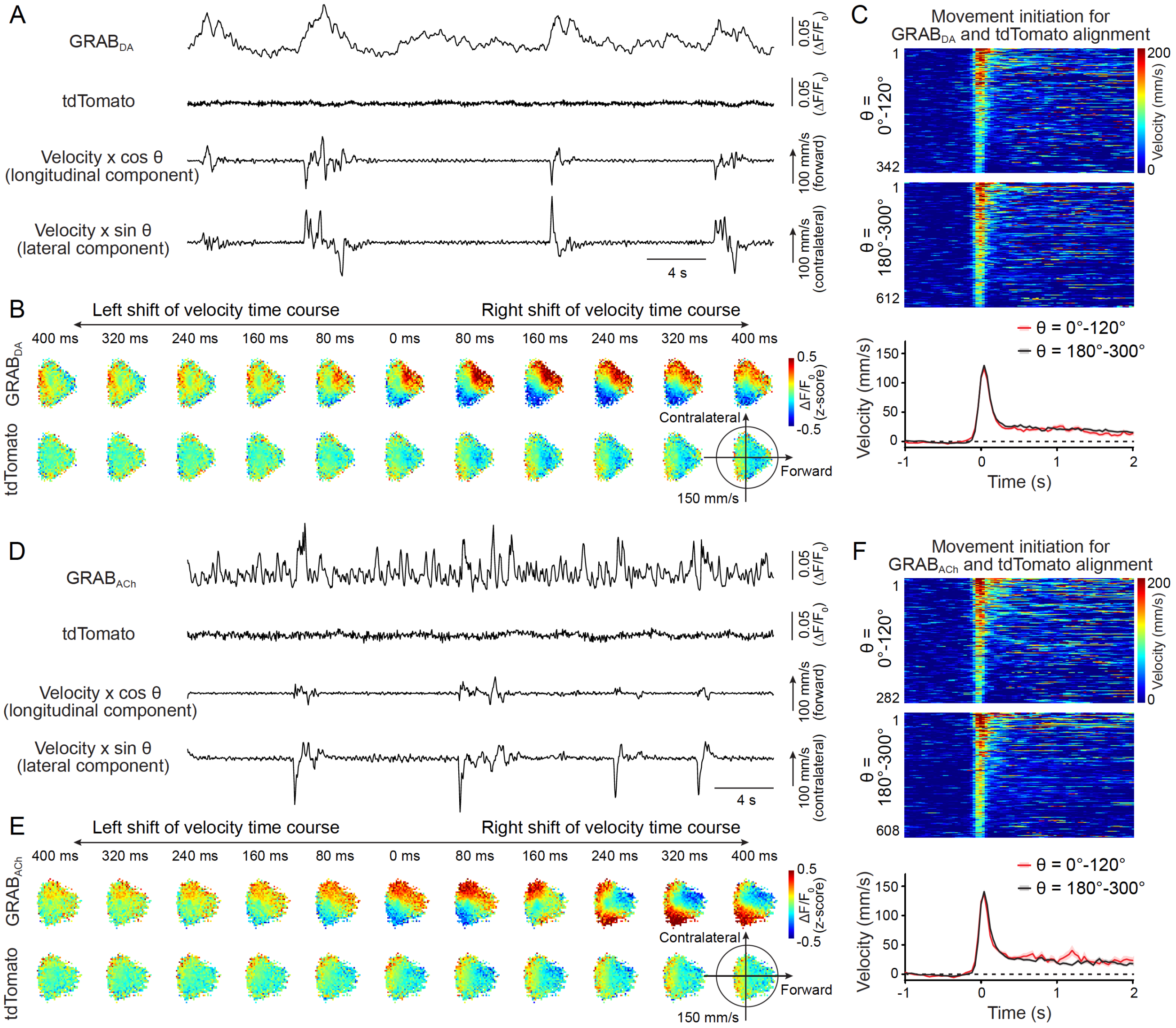

Fig. S10. Striatal dopamine and ACh levels are correlated with movement direction. (**A**) Example traces of GRAB$_{DA}$, tdTomato, and snout velocity. The velocity was decomposed as longitudinal and lateral components, and forward and contralateral directions were defined as positive directions in movement analyses. (**B**) Average GRAB$_{DA}$ and tdTomato signals registered to the artificially shifted velocity in polar coordinates. Stronger correlations between GRAB$_{DA}$ and movement direction were observed when the velocity time series was right-shifted, indicating that movement precedes GRAB$_{DA}$ peaks; n = 10 mice. (**C**) Individual (top, heatmap) and average (bottom) time courses of velocity amplitude during movement initiations used for the alignment of GRAB$_{DA}$ and tdTomato fluorescence. The average velocity amplitude before movement onset (40–1000 ms before the onset) was subtracted before plotting; n = 342 events/10 mice for $\theta = 0^\circ$–120°, 612/10 for $\theta = 180^\circ$–300°. (**D to F**) As A to C, but for GRAB_{ACh} signals. GRAB_{ACh} exhibited a stronger correlation with movement direction when the velocity time series was right-shifted, and the relationship was inverted when the shift exceeded 320 ms (Fig. 4F); n = 282/11 for $\theta = 0^\circ$–120°, 608/11 for $\theta = 180^\circ$–300°. Data are mean ± SEM; Mann-Whitney rank-sum test for areas under the curve (0–400 ms) in (C) and (F).

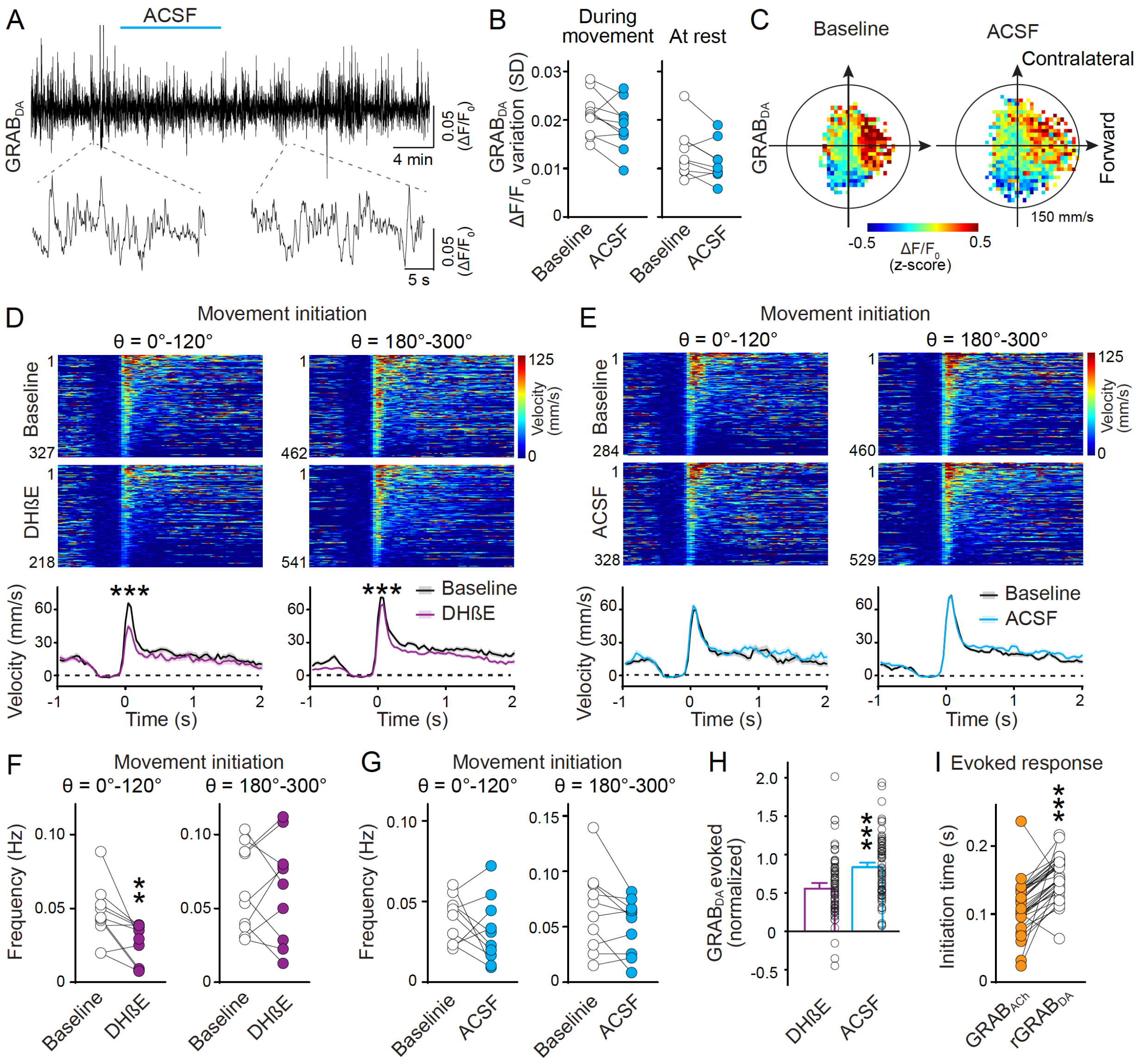

Fig. S11. Local inhibition of nAChRs in the striatum reduces movement initiation towards the contralateral side. (**A, B**) Example trace (A) and quantification (B, standard deviation, SD, of ΔF/F$_0$) of GRAB$_{DA}$ fluorescence variation before and after local delivery of ACSF (1 µl) to the recording site via the optofluid canula. Despite the apparent tendency towards a reduced variation, no significant change was detected; n = 10 mice. (**C**) Average GRAB$_{DA}$ signals registered to the concurrent velocity in polar coordinates before and after ACSF application; n = 10. (**D**) Individual (top, heatmap) and average (bottom) time course of velocity amplitude during movement initiations before and after local infusion of DHβE into the right dorsal striatum at the recording site. Basal levels of velocity amplitude (40-400 ms before the onset) were subtracted before plotting. DHβE infusion caused a significant reduction in the velocity amplitude of movement initiations with both $\theta = 0^\circ$–120° and $\theta = 180^\circ$–300°; $n = 327$ events/10 mice for baseline, 218/10 for DHβE with $\theta = 0^\circ$–120°; 462/10 for baseline, 541/10 for DHβE with $\theta = 180^\circ$–300°. (**E**) As (D), but for local infusion of ACSF. ACSF infusion caused no change in the velocity amplitudes in either direction; $n = 284/11$ for baseline, 328/11 for ACSF with $\theta = 0^\circ$–120°; 460/11 for baseline, 529/11 for ACSF with $\theta = 180^\circ$–300°. (**F**) Effects of DHβE on the frequency of movement initiations. DHβE reduced the frequency of movement initiations within $\theta = 0^\circ$–120° but not $\theta = 180^\circ$–300°; $n = 10$ mice each. (**G**) As F, but for local infusion of ACSF. No significant change was observed in the frequency of movement initiations in either direction; $n = 10$. (**H**) Comparison of relative changes in light-evoked GRAB$_{\mathrm{DA}}$ responses after local infusion of DHβE or ACSF; $n = 66$ responses/10 mice for DHβE, 72/10 for ACSF. (**I**) Comparison of initiation times (time point for the fastest rise within 400 ms after the start of the stimulation) in light-evoked responses of simultaneously recorded rGRAB$_{\mathrm{DA}}$ and GRAB$_{\mathrm{ACh}}$ fluorescence changes in the dorsal striatum. Only responses that exhibited an increase of z-score > 0.5 within 200 ms following the start of the light stimulus were included in the analyses. GRAB$_{\mathrm{ACh}}$ responses preceded those of rGRAB$_{\mathrm{DA}}$; $n = 34$ responses/4 mice. Data are mean ± SEM; *** $p < 0.001$, ** $p < 0.01$; Mann-Whitney rank-sum tests for areas under the curve (0–400 ms) for (D), (E), and (H); Wilcoxon signed-rank tests for (B), (F), (G), and (I).

References and Notes

1. W. Matsuda, T. Furuta, K. C. Nakamura, H. Hioki, F. Fujiyama, R. Arai, T. Kaneko, Single nigrostriatal dopaminergic neurons form widely spread and highly dense axonal arborizations in the neostriatum. *J. Neurosci.* **29**, 444–453 (2009).

2. J. D. Berke, What does dopamine mean? *Nat. Neurosci.* **21**, 787–793 (2018).

3. C. Liu, P. Goel, P. S. Kaeser, Spatial and temporal scales of dopamine transmission. *Nat. Rev. Neurosci.* **22**, 345–358 (2021).

4. E. S. Bromberg-Martin, M. Matsumoto, O. Hikosaka, Dopamine in motivational control: Rewarding, aversive, and alerting. *Neuron* **68**, 815–834 (2010).

5. C. J. Wilson, The mechanism of intrinsic amplification of hyperpolarizations and spontaneous bursting in striatal cholinergic interneurons. *Neuron* **45**, 575–585 (2005).

6. S. Threlfell, T. Lalic, N. J. Platt, K. A. Jennings, K. Deisseroth, S. J. Cragg, Striatal dopamine release is triggered by synchronized activity in cholinergic interneurons. *Neuron* **75**, 58–64 (2012).

7. N. Le Novère, M. Zoli, J.-P. Changeux, Neuronal nicotinic receptor alpha 6 subunit mRNA is selectively concentrated in catecholaminergic nuclei of the rat brain. *Eur. J. Neurosci.* **8**, 2428–2439 (1996).

8. I. W. Jones, J. P. Bolam, S. Wonnacott, Presynaptic localisation of the nicotinic acetylcholine receptor beta2 subunit immunoreactivity in rat nigrostriatal dopaminergic neurones. *J. Comp. Neurol.* **439**, 235–247 (2001).

9. M. F. Giorguieff, M. L. Le Floc'h, J. Glowinski, M. J. Besson, Involvement of cholinergic presynaptic receptors of nicotinic and muscarinic types in the control of the spontaneous release of dopamine from striatal dopaminergic terminals in the rat. *J. Pharmacol. Exp. Ther.* **200**, 535–544 (1977).

10. F.-M. Zhou, Y. Liang, J. A. Dani, Endogenous nicotinic cholinergic activity regulates dopamine release in the striatum. *Nat. Neurosci.* **4**, 1224–1229 (2001).

11. R. Cachope, Y. Mateo, B. N. Mathur, J. Irving, H.-L. Wang, M. Morales, D. M. Lovinger, J. F. Cheer, Selective activation of cholinergic interneurons enhances accumbal phasic dopamine release: Setting the tone for reward processing. *Cell Rep.* **2**, 33–41 (2012).

12. L. Wang, X. Zhang, H. Xu, L. Zhou, R. Jiao, W. Liu, F. Zhu, X. Kang, B. Liu, S. Teng, Q. Wu, M. Li, H. Dou, P. Zuo, C. Wang, S. Wang, Z. Zhou, Temporal components of cholinergic terminal to dopaminergic terminal transmission in dorsal striatum slices of mice. *J. Physiol.* **592**, 3559–3576 (2014).

13. F. Sun, J. Zhou, B. Dai, T. Qian, J. Zeng, X. Li, Y. Zhuo, Y. Zhang, Y. Wang, C. Qian, K. Tan, J. Feng, H. Dong, D. Lin, G. Cui, Y. Li, Next-generation GRAB sensors for monitoring dopaminergic activity in vivo. *Nat. Methods* **17**, 1156–1166 (2020).

14. C. Liu, L. Kershberg, J. Wang, S. Schneeberger, P. S. Kaeser, Dopamine Secretion Is Mediated by Sparse Active Zone-like Release Sites. *Cell* **172**, 706–718.e15 (2018).

15. M. Jing, Y. Li, J. Zeng, P. Huang, M. Skirzewski, O. Kljakic, W. Peng, T. Qian, K. Tan, J. Zou, S. Trinh, R. Wu, S. Zhang, S. Pan, S. A. Hires, M. Xu, H. Li, L. M. Saksida, V. F.

Prado, T. J. Bussey, M. A. M. Prado, L. Chen, H. Cheng, Y. Li, An optimized acetylcholine sensor for monitoring in vivo cholinergic activity. *Nat. Methods* **17**, 1139–1146 (2020).

16. A. A. Mamaligas, C. P. Ford, Spontaneous synaptic activation of muscarinic receptors by striatal cholinergic neuron firing. *Neuron* **91**, 574–586 (2016).
17. J. M. Schulz, M. J. Oswald, J. N. J. Reynolds, Visual-induced excitation leads to firing pauses in striatal cholinergic interneurons. *J. Neurosci.* **31**, 11133–11143 (2011).
18. G. Morris, D. Arkadir, A. Nevet, E. Vaadia, H. Bergman, Coincident but distinct messages of midbrain dopamine and striatal tonically active neurons. *Neuron* **43**, 133–143 (2004).
19. Y. Cai, C. P. Ford, Dopamine cells differentially regulate striatal cholinergic transmission across regions through corelease of dopamine and glutamate. *Cell Rep.* **25**, 3148–3157.e3 (2018).
20. C. Straub, N. X. Tritsch, N. A. Hagan, C. Gu, B. L. Sabatini, Multiphasic modulation of cholinergic interneurons by nigrostriatal afferents. *J. Neurosci.* **34**, 8557–8569 (2014).
21. H. T. Chang, Dopamine-acetylcholine interaction in the rat striatum: A dual-labeling immunocytochemical study. *Brain Res. Bull.* **21**, 295–304 (1988).
22. D. B. Pereira, Y. Schmitz, J. Mészáros, P. Merchant, G. Hu, S. Li, A. Henke, J. E. Lizardi-Ortiz, R. J. Karpowicz Jr., T. J. Morgenstern, M. S. Sonders, E. Kanter, P. C. Rodriguez, E. V. Mosharov, D. Sames, D. Sulzer, Fluorescent false neurotransmitter reveals functionally silent dopamine vesicle clusters in the striatum. *Nat. Neurosci.* **19**, 578–586 (2016).
23. E. R. Decker, J. A. Dani, Calcium permeability of the nicotinic acetylcholine receptor: The single-channel calcium influx is significant. *J. Neurosci.* **10**, 3413–3420 (1990).
24. R. G. Held, C. Liu, K. Ma, A. M. Ramsey, T. B. Tarr, G. De Nola, S. S. H. Wang, J. Wang, A. M. J. M. van den Maagdenberg, T. Schneider, J. Sun, T. A. Blanpied, P. S. Kaeser, Synapse and active zone assembly in the absence of presynaptic Ca^{2+} channels and Ca^{2+} entry. *Neuron* **107**, 667–683.e9 (2020).
25. J. Yang, Y. Xiao, L. Li, Q. He, M. Li, Y. Shu, Biophysical properties of somatic and axonal voltage-gated sodium channels in midbrain dopaminergic neurons. *Front. Cell. Neurosci.* **13**, 317 (2019).
26. A. Ritzau-Jost, T. Tsintsadze, M. Krueger, J. Ader, I. Bechmann, J. Eilers, B. Barbour, S. M. Smith, S. Hallermann, Large, Stable spikes exhibit differential broadening in excitatory and inhibitory neocortical boutons. *Cell Rep.* **34**, 108612 (2021).
27. M. Howe, I. Ridouh, A. L. Allegra Mascaro, A. Larios, M. Azcorra, D. A. Dombeck, Coordination of rapid cholinergic and dopaminergic signaling in striatum during spontaneous movement. *eLife* **8**, e44903 (2019).
28. P. D. Dodson, J. K. Dreyer, K. A. Jennings, E. C. J. Syed, R. Wade-Martins, S. J. Cragg, J. P. Bolam, P. J. Magill, Representation of spontaneous movement by dopaminergic neurons is cell-type selective and disrupted in parkinsonism. *Proc. Natl. Acad. Sci. U.S.A.* **113**, E2180–E2188 (2016).

29. S. Kaneko, T. Hikida, D. Watanabe, H. Ichinose, T. Nagatsu, R. J. Kreitman, I. Pastan, S. Nakanishi, Synaptic integration mediated by striatal cholinergic interneurons in basal ganglia function. *Science* **289**, 633–637 (2000).

30. M. W. Howe, D. A. Dombeck, Rapid signalling in distinct dopaminergic axons during locomotion and reward. *Nature* **535**, 505–510 (2016).

31. J. A. da Silva, F. Tecuapetla, V. Paixão, R. M. Costa, Dopamine neuron activity before action initiation gates and invigorates future movements. *Nature* **554**, 244–248 (2018).

32. T. Dugladze, D. Schmitz, M. A. Whittington, I. Vida, T. Gloveli, Segregation of axonal and somatic activity during fast network oscillations. *Science* **336**, 1458–1461 (2012).

33. M. E. J. Sheffield, T. K. Best, B. D. Mensh, W. L. Kath, N. Spruston, Slow integration leads to persistent action potential firing in distal axons of coupled interneurons. *Nat. Neurosci.* **14**, 200–207 (2011).

34. J. A. Dani, D. Bertrand, Nicotinic acetylcholine receptors and nicotinic cholinergic mechanisms of the central nervous system. *Annu. Rev. Pharmacol. Toxicol.* **47**, 699–729 (2007).

35. N. Eshel, J. Tian, M. Bukwich, N. Uchida, Dopamine neurons share common response function for reward prediction error. *Nat. Neurosci.* **19**, 479–486 (2016).

36. J. G. Parker, L. S. Zweifel, J. J. Clark, S. B. Evans, P. E. M. Phillips, R. D. Palmiter, Absence of NMDA receptors in dopamine neurons attenuates dopamine release but not conditioned approach during Pavlovian conditioning. *Proc. Natl. Acad. Sci. U.S.A.* **107**, 13491–13496 (2010).

37. A. A. Grace, B. S. Bunney, Nigral dopamine neurons: Intracellular recording and identification with L-dopa injection and histofluorescence. *Science* **210**, 654–656 (1980).

38. L. J. Gentet, S. R. Williams, Dopamine gates action potential backpropagation in midbrain dopaminergic neurons. *J. Neurosci.* **27**, 1892–1901 (2007).

39. N. F. Parker, C. M. Cameron, J. P. Taliaferro, J. Lee, J. Y. Choi, T. J. Davidson, N. D. Daw, I. B. Witten, Reward and choice encoding in terminals of midbrain dopamine neurons depends on striatal target. *Nat. Neurosci.* **19**, 845–854 (2016).

40. C. Liu, Data table for an action potential initiation mechanism in distal axons for the control of dopamine release. Zenodo (2022); doi:10.5281/zenodo.6342359.

41. C. Liu, Matlab script for object recognition and analysis. Zenodo (2022); doi:10.5281/zenodo.6342367.

42. C. M. Bäckman, N. Malik, Y. Zhang, L. Shan, A. Grinberg, B. J. Hoffer, H. Westphal, A. C. Tomac, Characterization of a mouse strain expressing Cre recombinase from the 3′ untranslated region of the dopamine transporter locus. *Genesis* **44**, 383–390 (2006).

43. J. Rossi, N. Balthasar, D. Olson, M. Scott, E. Berglund, C. E. Lee, M. J. Choi, D. Lauzon, B. B. Lowell, J. K. Elmquist, Melanocortin-4 receptors expressed by cholinergic neurons regulate energy balance and glucose homeostasis. *Cell Metab.* **13**, 195–204 (2011).

44. L. Madisen, T. Mao, H. Koch, J. M. Zhuo, A. Berenyi, S. Fujisawa, Y.-W. A. Hsu, A. J. Garcia 3rd, X. Gu, S. Zanella, J. Kidney, H. Gu, Y. Mao, B. M. Hooks, E. S. Boyden, G.

Buzsáki, J. M. Ramirez, A. R. Jones, K. Svoboda, X. Han, E. E. Turner, H. Zeng, A toolbox of Cre-dependent optogenetic transgenic mice for light-induced activation and silencing. *Nat. Neurosci.* **15**, 793–802 (2012).

45. B. Todorov, R. C. G. van de Ven, S. Kaja, L. A. M. Broos, S. J. Verbeek, J. J. Plomp, M. D. Ferrari, R. R. Frants, A. M. J. M. van den Maagdenberg, Conditional inactivation of the Cacna1a gene in transgenic mice. *Genesis* **44**, 589–594 (2006).
46. A. Pereverzev, M. Mikhna, R. Vajna, C. Gissel, M. Henry, M. Weiergräber, J. Hescheler, N. Smyth, T. Schneider, Disturbances in glucose-tolerance, insulin-release, and stress-induced hyperglycemia upon disruption of the Ca(v)2.3 (α1E) subunit of voltage-gated Ca^{2+} channels. *Mol. Endocrinol.* **16**, 884–895 (2002).
47. M. G. L. Gustafsson, L. Shao, P. M. Carlton, C. J. R. Wang, I. N. Golubovskaya, W. Z. Cande, D. A. Agard, J. W. Sedat, Three-dimensional resolution doubling in wide-field fluorescence microscopy by structured illumination. *Biophys. J.* **94**, 4957–4970 (2008).
48. A. Mathis, P. Mamidanna, K. M. Cury, T. Abe, V. N. Murthy, M. W. Mathis, M. Bethge, DeepLabCut: Markerless pose estimation of user-defined body parts with deep learning. *Nat. Neurosci.* **21**, 1281–1289 (2018).